PCANet: An energy perspective

Jiasong Wu, Shijie Qiu, Youyong Kong, Longyu Jiang, Yang Chen, Wankou Yang, Lotfi Senhadji, Huazhong Shu

PCANet: An energy perspective

Jiasong Wu[1, 2, 4], Shijie Qiu[1, 4], Youyong Kong[1, 4], Longyu Jiang[1, 4],
Yang Chen[1, 4], Wankou Yang[5], Lotfi Senhadji[3, 4], Huazhong Shu[1, 2, 4]

[1]LIST, Key Laboratory of Computer Network and Information Integration, Southeast University, Ministry of Education, Nanjing 210096, China

[2]International Joint Research Laboratory of Information Display and Visualization, Southeast University, Ministry of Education, Nanjing 210096, China

[3]Univ Rennes, INSERM, LTSI - UMR 1099, F-35000 Rennes, France

[4]Centre de Recherche en Information Biomédicale Sino-français (CRIBs), SEU, Univ Rennes, INSERM, Nanjing 210096, China

[5]School of Automation, Southeast University, Nanjing 210096, China

Abstract

The principal component analysis network (PCANet), which is one of the recently proposed deep learning architectures, achieves the state-of-the-art classification accuracy in various databases. However, the visualization or explanation of the PCANet is lacked. In this paper, we try to explain why PCANet works well from energy perspective point of view based on a set of experiments. The paper shows that the error rate of PCANet is qualitatively correlated with the inverse of the logarithm of BlockEnergy, which is the energy after the block sliding process of PCANet, and also this relation is quantified by using curve fitting method. The proposed energy explanation approach can also be used as a testing method for checking if every step of the constructed networks is necessary.

Keywords

Deep learning; Convolutional neural networks; PCANet; Error rate; Energy; Image recognition

1. Introduction

Deep learning [1-10], especially convolutional neural networks (CNNs) [11, 12], is a hot research topic that achieves the state-of-the-art results in many image classification tasks, including ImageNet large scale visual recognition [13-17], Labeled Faces in the Wild (LFW) face recognition [18-20], handwritten digit recognition [11, 21], and other applications [22-31], etc. The great success of deep learning systems is impressive, but a fundamental question still remains: Why do they work [32]? In the recent years, several attempts have been made for explaining the deep learning systems. These attempts can be roughly categorized into two classes: theoretical explanation and experimental explanation.

Theoretical explanation method tries to elucidate deep learning systems by using various theories, which can be classified into seven subclasses: *1) Renormalization Theory*. Mehta and Schwab [33] constructed an exact mapping from the variational renormalization group (RG) scheme [34] to deep neural networks (DNNs) based on Restricted Boltzmann Machines (RBMs) [1, 2], and thus explained DNNs as a RG-like procedure to extract relevant features from structured data. *2) Probabilistic Theory*. Patel *et al*. [32] developed a new probabilistic framework for deep learning based on a Bayesian generative probabilistic model. By relaxing the generative model to a discriminative one, their models recover two of the current leading deep learning systems: deep CNNs and random decision forests (RDFs). *3) Information Theory*. Tishby and Zaslavsky [35] analyzed DNNs via the theoretical framework of the information bottleneck principle. Steeg and Galstyan [36] further introduced a framework for unsupervised learning of deep representations based on a hierarchical decomposition of information. *4) Developmental robotic perspective.* Sigaud and Droniou [37] scrutinized deep learning techniques under the light of their capability to construct a hierarchy of multimodal representations from the raw sensors of robots. *5) Geometric viewpoint*. Lei *et al*. [38] showed the intrinsic relations between optimal transportation and convex geometry and gave a geometric interpretation to generative models. Dong *et al*. [39] draw a geometric picture of the deep learning system by finding its analogies with two existing geometric structures, the geometry of quantum computations and the geometry of the diffeomorphic template matching. *6) Group Theory.* Paul and Venkatasubramanian [40] explained deep learning system from the group-theoretic perspective point of view and showed why higher layers of deep learning framework tend to learn more abstract features. Shaham *et al*. [41] discussed the approximation of wavelet functions using deep neural nets. Anselmi *et al*. [42] explained deep CNNs by invariant and selective theory, whose ideas come from *i*-Theory [43], which is a

recent theory of feedforward processing in sensory cortex. *7) Energy perspective.* The mathematical analysis of CNNs was performed by Mallat in [44], where wavelet scattering network (ScatNet) was proposed. The convolutional layer, nonlinear layer, pooling layer were constructed by prefixed complex wavelets, modulus operator, and average operator, respectively. Owning to its characteristic of using prefixed filters which are not learned from data, ScatNet was explained in [44] from *energy perspective* both in theory and experiment aspect, that is, **ScatNet maintains the energy of image in each layer although using modulus operator.** ScatNet achieves the state-of-the-art results in various image classification tasks [45] and was then extended to semi-discrete frame networks [46] as well as complex valued convolutional nets [47].

Experimental explanation methods tend to understand deep learning systems by inverting them to visualize the "filters" learned by the model [48]. For example, Larochelle *et al*. [49] presented a series of experiments on Deep Belief Networks (DBN) [1] and stacked autoencoder networks [3] by using artificial data and indicate that these models show promise in solving harder learning problems that exhibit many factors of variation. Goodfellow *et al*. [50] examined the invariances of stacked autoencoder networks [3] and also convolutional deep belief networks (CDBNs) [4] by using natural images and natural video sequences. Erhan *et al*. [48] studied three filter visualization methods (Maximizing the activation, Sampling from a unit of a network, Linear combination of previous layers' filters) on DBN [1] and Stacked Denoising Autoencoders [5]. Szegedy *et al*. [51] reported two intriguing properties of deep neural networks. Zeiler and Fergus [52] proposed DeConvNet method in which the network computations were backtracked to identify which image patches are responsible for certain neural activations. DeConvNet uses AlexNet [11] as an example to observe the evolution of features during training and to diagnose potential problems by using such a model. Simonyan *et al*. [53] demonstrated how saliency maps can be obtained from a Convnet by projecting back from the fully connected layers of the network. Girshick *et al.* [54] showed visualizations that identify patches within a dataset that are responsible for strong activations at higher layers in the model. Mahendran and Vedaldi [55] gave a general framework to invert CNNs and they tried to answer the following question: given an encoding of an image, to which extent is it possible to reconstruct the image itself?

Recently, Chan *et al*. [56] proposed a new deep learning algorithm called principal component analysis network (PCANet), whose convolutional layer, nonlinear processing layer, and feature pooling layer consist of principal component analysis (PCA) filter bank, binarization, and block-wise histogram, respectively. Chan *et al*. [56] also

visualize the filters of PCANet like in [48] and [52]. Although PCANet is constructed with most basic units, it surprisingly achieves the state-of-the-art performance for most image classification tasks. PCANet arouses the interest of many researchers in this field. For example, Gan *et al*. proposed a graph embedding network (GENet) [57] for image classification. Wang and Tan [58] presented a C-SVDDNet for unsupervised feature learning. Feng *et al*. [59] presented a discriminative locality alignment network (DLANet) for scene classification. Ng and Teoh [60] proposed discrete cosine transform network (DCTNet) for face recognition. Gan *et al*. [61] presented a PCA-based convolutional network by combining the structure of PCANet and the LeNet-5 [11, 12]. Zhao *et al*. [62] proposed multi-level modified finite radon transform network (MMFRTN) for image upsampling. Lei *et al*. [63] developed stacked image descriptor for face recognition. Li *et al*. [64] proposed SAE-PCA network for human gesture recognition in RGBD (Red, Green, Blue, Depth) images. Zeng *et al*. [65] proposed a quaternion principal component analysis network (QPCANet) for color image classification. Wu *et al*. [66] proposed a multilinear principal component analysis network (MPCANet) for tensor object classification. Although PCANet has been extensively investigated, the question still remains: Why it works well by using the most basic and simple units? To the best of our knowledge, no attempt to explain every step of the PCANet is available in the literature.

In this paper, 1) We present a new way to visualize, explain and understand every step of PCANet from an *energy perspective* on experiment aspect by using five image databases: Yale database [67], AR database [68], CMU PIE face database [69], ORL database [70], and CIFAR-10 database [71]. The proposed energy explanation approach can provide more information than the filter visualization method reported in [56]; 2) We shows qualitatively that the error rate of PCANet is correlated with the inverse of the logarithm of **BlockEnergy**, which is the energy after the block sliding process of PCANet, and then we try to find quantitatively their relations by using curve fitting method; 3) we show that the proposed energy explanation approach can be used as a testing method for checking if every step of the constructed networks is necessary; and 4) The energy explanation approach proposed in this paper can be extended to other PCANet-based networks [57-66].

The paper is organized as follows. PCANet is reviewed in section 2. Section 3 presents an energy method to visualize, explain and understand every step of PCANet. Discussion is given in Section 4 and Section 5 concludes the work.

2. Review of Principal Component Analysis Network

In this section, we first review the PCANet [56], whose architecture is shown in Fig. 1 and can be divided into three stages, including 10 steps. Suppose that we have N input training images $\{\mathbf{I}_i, i=1,2,...,N\}$, $\mathbf{I}_i \in \mathbb{R}^{m\times n}$, and that the patch size (or two-dimensional filter size) of all stages is $k_1\times k_2$, where k_1 and k_2 are odd integers satisfying $1\le k_1\le m$, $1\le k_2\le n$. We further assume that the number of filters in layer i is L_i, that is, L_1 for the first stage and L_2 for the second stage. In the following, we describe the structure of PCANet in detail.

Let the N input images $\{\mathbf{I}_i, i=1,2,...,N\}$ be concatenated as follows:

$$\mathbf{I}=\begin{bmatrix}\mathbf{I}_1 & \mathbf{I}_2 & \cdots & \mathbf{I}_N\end{bmatrix}\in\mathbb{R}^{m\times Nn}. \tag{1}$$

2.1. The first stage of PCANet

As shown in Fig. 1, the first stage of PCANet includes the following 3 steps:

Step 1: the first patch sliding process.

The images are padded to $\mathbf{I}'_i \in \mathbb{R}^{(m+k_1-1)\times(n+k_2-1)}$ before sliding operation. Out-of-range input pixels are taken to be zero. This can ensure all weights in the filters reach the entire images. We use a patch of size $k_1\times k_2$ to slide each pixel of the ith image $\mathbf{I}'_i \in \mathbb{R}^{(m+k_1-1)\times(n+k_2-1)}$, then reshape each $k_1\times k_2$ matrix into a column vector, which is then concatenated to obtain a matrix

$$\mathbf{X}_i=\begin{bmatrix}\mathbf{x}_{i,1} & \mathbf{x}_{i,2} & \cdots & \mathbf{x}_{i,mn}\end{bmatrix}\in\mathbb{R}^{k_1k_2\times mn}, i=1,2,...,N, \tag{2}$$

where $\mathbf{x}_{i,j}$ denotes the jth vectorized patch in $\mathbf{I}_i$.

Therefore, for all the input training images $\{\mathbf{I}_i, i=1,2,...,N\}$, we can obtain the following matrix

$$\mathbf{X}=\begin{bmatrix}\mathbf{X}_1 & \mathbf{X}_2 & \cdots & \mathbf{X}_N\end{bmatrix}\in\mathbb{R}^{k_1k_2\times Nmn}, \tag{3}$$

Step 2: the first mean remove process.

In this step, we subtract patch mean from each patch and obtain

$$\bar{\mathbf{X}}_i=\begin{bmatrix}\bar{\mathbf{x}}_{i,1} & \bar{\mathbf{x}}_{i,2} & \cdots & \bar{\mathbf{x}}_{i,mn}\end{bmatrix}\in\mathbb{R}^{k_1k_2\times mn}, i=1,2,...,N, \tag{4}$$

where $\bar{\mathbf{x}}_{i,j}=\mathbf{x}_{i,j}-\frac{1}{mn}\sum_{j=1}^{mn}\mathbf{x}_{i,j}$, is a mean-removed vector.

For each input training image $\mathbf{I}_i \in \mathbb{R}^{m\times n}$, we can get a substituted matrix $\bar{\mathbf{X}}_i \in \mathbb{R}^{k_1k_2\times mn}$. Thus, for all the input training images $\{\mathbf{I}_i, i=1,2,...,N\}$, we can obtain the following matrix

$$\bar{\mathbf{X}} = \left[\bar{\mathbf{X}}_1 \quad \bar{\mathbf{X}}_2 \quad \cdots \quad \bar{\mathbf{X}}_N\right] \in \mathbb{R}^{k_1k_2\times Nmn}. \tag{5}$$

Step 3: the first PCA process.

In this step, we get the eigenvalues and eigenvectors of $\bar{\mathbf{X}}$ in (5) by using PCA algorithm, which in fact minimizes the reconstruction error in Frobenius norm as follows:

$$\min_{\mathbf{U}\in\mathbb{R}^{k_1k_2\times L_1}} \left\|\bar{\mathbf{X}} - \mathbf{U}\mathbf{U}^T\bar{\mathbf{X}}\right\|_F^2, \text{ s.t. } \mathbf{U}^T\mathbf{U} = \mathbf{D}_{L_1}, \tag{6}$$

where $\mathbf{D}_{L_1}$ is an identity matrix of size $L_1\times L_1$, and the superscript T denotes transposition. Eq. (6) can be solved by eigenvalue decomposition method shown in Appendix. The PCA filter of the first stage of PCANet is then obtained from (A.5) by

$$\mathbf{W}_l^I = \text{mat}_{k_1,k_2}(\mathbf{u}_l) \in \mathbb{R}^{k_1\times k_2}, l=1,2,\ldots,L_1, \tag{7}$$

where $\text{mat}_{k_1,k_2}(\mathbf{u}_l)$ is a function that maps $\mathbf{u}_l \in \mathbb{R}^{k_1k_2}$ to a matrix $\mathbf{W}_l^I \in \mathbb{R}^{k_1\times k_2}$. Note that the superscript of capital Roman number I denotes the first stage,

The output of the first stage of PCANet is given by

$$\mathbf{I}_{i,l}^I = \mathbf{I}_i * \mathbf{W}_l^I \in \mathbb{R}^{m\times n}, \quad l=1,2,...,L_1; \quad i=1,2,\ldots,N, \tag{8}$$

where $*$ denotes two-dimensional (2-D) convolution, and the boundary of $\mathbf{I}_i$ is zero-padded before convolving with $\mathbf{W}_l^I$ in order to make $\mathbf{I}_{i,l}^I$ having the same size as $\mathbf{I}_i$.

For each input image $\mathbf{I}_i \in \mathbb{R}^{m\times n}$, we obtain L_1 output images $\{\mathbf{I}_{i,l}^I, l=1,2,...,L_1\}, \mathbf{I}_{i,l}^I \in \mathbb{R}^{m\times n}$ after the first stage of PCANet. We denote $\mathbf{I}^I$ as

$$\mathbf{I}^I = \left[\mathbf{I}_{1,1}^I \quad \cdots \quad \mathbf{I}_{1,L_1}^I \quad \cdots \quad \mathbf{I}_{N,1}^I \quad \cdots \quad \mathbf{I}_{N,L_1}^I\right] \in \mathbb{R}^{m\times NL_1n}. \tag{9}$$

2.2. The second stage of PCANet

As shown in Fig. 1, the second stage of PCANet also includes 3 steps:

Step 4: the second patch sliding process.

Similar to *Step 1*, we use a patch of size $k_1 \times k_2$ to slide each pixel of the ith image $\mathbf{I}_{i,l}^I \in \mathbb{R}^{k_1 \times k_2}, l = 1, 2, ..., L_1$, and obtain a matrix

$$\mathbf{Y}_{i,l} = \left[\mathbf{y}_{i,l,1} \quad \mathbf{y}_{i,l,2} \quad \cdots \quad \mathbf{y}_{i,l,mn} \right] \in \mathbb{R}^{k_1 k_2 \times mn},\ l = 1, 2, ..., L_1;\ i = 1, 2, ..., N, \tag{10}$$

where $\mathbf{y}_{i,l,j}$ denotes the jth vectorized patch in $\mathbf{I}_{i,l}^I$.

Therefore, for the ith filter, all the input training images $\left\{ \mathbf{I}_{i,l}^I, i = 1, 2, ..., N \right\}$, we can obtain the following matrix

$$\mathbf{Y}_l = \left[\mathbf{Y}_{1,l} \quad \mathbf{Y}_{2,l} \quad \cdots \quad \mathbf{Y}_{N,l} \right] \in \mathbb{R}^{k_1 k_2 \times Nmn}, \tag{11}$$

We concatenate the matrices of all the L_1 filters and obtain

$$\mathbf{Y} = \left[\mathbf{Y}_1 \quad \mathbf{Y}_2 \quad \cdots \quad \mathbf{Y}_{L_1} \right] \in \mathbb{R}^{k_1 k_2 \times L_1 Nmn}. \tag{12}$$

Step 5: the second mean remove process.

Similar to *Step 2*, we obtain the mean-removed version of (12) by

$$\bar{\mathbf{Y}} = \left[\bar{\mathbf{Y}}_1 \quad \bar{\mathbf{Y}}_2 \quad \cdots \quad \bar{\mathbf{Y}}_{L_1} \right] \in \mathbb{R}^{k_1 k_2 \times L_1 Nmn}, l = 1, 2, ..., L_1, \tag{13}$$

where

$$\bar{\mathbf{Y}}_l = \left[\bar{\mathbf{Y}}_{1,l} \quad \bar{\mathbf{Y}}_{2,l} \quad \cdots \quad \bar{\mathbf{Y}}_{N,l} \right] \in \mathbb{R}^{k_1 k_2 \times Nmn}, \tag{14}$$

$$\bar{\mathbf{Y}}_{i,l} = \left[\bar{\mathbf{y}}_{i,l,1} \quad \bar{\mathbf{y}}_{i,l,2} \quad \cdots \quad \bar{\mathbf{y}}_{i,l,mn} \right] \in \mathbb{R}^{k_1 k_2 \times mn},\ l = 1, 2, ..., L_1;\ i = 1, 2, ..., N, \tag{15}$$

$$\bar{\mathbf{y}}_{i,l,j} = \mathbf{y}_{i,l,j} - \frac{1}{mn} \sum_{j=1}^{mn} \mathbf{y}_{i,l,j}, l = 1, 2, ..., L_1;\ i = 1, 2, ..., N. \tag{16}$$

Step 6: the second PCA process.

Similar to *Step 3*, we use the PCA algorithm to minimize the following optimization problem:

$$\min_{\mathbf{V} \in \mathbb{R}^{k_1 k_2 \times L_2}} \left\| \bar{\mathbf{Y}} - \mathbf{V}\mathbf{V}^T \bar{\mathbf{Y}} \right\|_F^2,\ \text{s.t. } \mathbf{V}^T \mathbf{V} = \mathbf{D}_{L_2}, \tag{17}$$

where $\mathbf{D}_{L_2}$ is an identity matrix of size $L_2 \times L_2$. Eq. (17) can also be solved by the eigenvalue decomposition method shown in Appendix in which we replace $\bar{\mathbf{X}}$, $\mathbf{U}$, $\mathbf{u}$, $\mathbf{C}_1$, L_1, N, $\lambda_i^I, i = 1, 2, ..., L_1$ by $\bar{\mathbf{Y}}$, $\mathbf{V}$, $\mathbf{v}$, $\mathbf{C}_2, L_2, L_1 N, \lambda_i^{II}, i = 1, 2, ..., L_2$, respectively. The PCA filter of the second stage of PCANet is then obtained from (A.5) by

$$\mathbf{W}_\ell^{II} = \text{mat}_{k_1, k_2}\left(\mathbf{v}_\ell \right) \in \mathbb{R}^{k_1 \times k_2}, \ell = 1, 2, \ldots, L_2, \tag{18}$$

where $\mathrm{mat}_{k_1,k_2}(\mathbf{v}_\ell)$ is a function that maps $\mathbf{v}_\ell \in \mathbb{R}^{k_1k_2}$ to a matrix $\mathbf{W}_\ell^{II} \in \mathbb{R}^{k_1\times k_2}$. Note that the italic superscript *II* in (18) denotes the second stage. Therefore, the output of the second stage of PCANet is given by

$$\mathbf{I}_{i,l,\ell}^{II} = \mathbf{I}_{i,l}^{I} * \mathbf{W}_\ell^{II} \in \mathbb{R}^{k_1\times k_2},\ \ l=1,2,...,L_1;\ \ell=1,2,...,L_2;\ \ i=1,2,\ldots,N, \tag{19}$$

where $*$ denotes 2-D convolution.

For each input image $\mathbf{I}_{i,l}^{I} \in \mathbb{R}^{m\times n}$, we obtain L_2 output images $\left\{\mathbf{I}_{i,l,\ell}^{II}, \ell=1,2,...,L_2\right\}, \mathbf{I}_{i,l,\ell}^{II} \in \mathbb{R}^{m\times n}$ after the second stage of PCANet. Thus, we obtain NL_1L_2 images $\left\{\mathbf{I}_{i,l,\ell}^{II},\ l=1,2,...,L_1;\ \ell=1,2,...,L_2;\ i=1,2,\ldots,N\right\}, \mathbf{I}_{i,l,\ell}^{II} \in \mathbb{R}^{m\times n}$, for all the input training images $\left\{\mathbf{I}_i, i=1,2,\ldots,N\right\}, \mathbf{I}_i \in \mathbb{R}^{m\times n}$ after the first and second stages.

We denote $\mathbf{I}^{II}$ as

$$\mathbf{I}^{II} = \left[\mathbf{I}_{1,1,1}^{II} \ \cdots\ \mathbf{I}_{1,1,L_2}^{II} \ \cdots\ \mathbf{I}_{1,L_1,1}^{II} \ \cdots\ \mathbf{I}_{1,L_1,L_2}^{II} \ \cdots\cdots\ \mathbf{I}_{N,1,1}^{II} \ \cdots\ \mathbf{I}_{N,1,L_2}^{II} \ \cdots\ \mathbf{I}_{N,L_1,1}^{II} \ \cdots\ \mathbf{I}_{N,L_1,L_2}^{II}\right]. \tag{20}$$

2.3. The output stage of PCANet

Step 7: binary quantization.

In this step, we binarize the outputs $\mathbf{I}_{i,l,\ell}^{II}$ of the second stage of PCANet and obtain

$$\mathbf{P}_{i,l,\ell} = H\left(\mathbf{I}_{i,l,\ell}^{II}\right), l=1,2,...,L_1;\ \ell=1,2,...,L_2;\ \ i=1,2,\ldots,N, \tag{21}$$

where $H(\cdot)$ is a Heaviside step function whose value is one for positive entries and zero otherwise. We denote $\mathbf{P}$ as

$$\mathbf{P} = \left[\mathbf{P}_{1,1,1} \ \cdots\ \mathbf{P}_{1,1,L_2} \ \cdots\ \mathbf{P}_{1,L_1,1} \ \cdots\ \mathbf{P}_{1,L_1,L_2} \ \cdots\cdots\ \mathbf{P}_{N,1,1} \ \cdots\ \mathbf{P}_{N,1,L_2} \ \cdots\ \mathbf{P}_{N,L_1,1} \ \cdots\ \mathbf{P}_{N,L_1,L_2}\right]. \tag{22}$$

Step 8: weight and sum.

Around each pixel, we view the vector of L_2binary bits as a decimal number. This converts the binary images $\left\{\mathbf{P}_{i,l,\ell}\right\}$ back into integer-valued images as follows:

$$\mathbf{T}_{i,l} = \sum_{\ell=1}^{L_2} 2^{\ell-1}\mathbf{P}_{i,l,\ell}, \tag{23}$$

We denote $\mathbf{T}$ as

$$\mathbf{T} = \left[\mathbf{T}_{1,1} \ \cdots\ \mathbf{T}_{1,L_1} \ \cdots\ \mathbf{T}_{N,1} \ \cdots\ \mathbf{T}_{N,L_1}\right] \in \mathbb{R}^{m\times NL_1n}. \tag{24}$$

Step 9: block sliding.

We use a block of size $h_1 \times h_2$ to slide each of the L_1 images $\mathbf{T}_{i,l}, l = 1,...,L_1,$ with overlap ratio R, and then reshape each $h_1 \times h_2$ matrix into a columnvector, which is then concatenated to obtain a matrix

$$\mathbf{Z}_{i,l} = \left[\mathbf{z}_{i,l,1} \quad \mathbf{z}_{i,l,2} \quad \cdots \quad \mathbf{z}_{i,l,B} \right] \in \mathbb{R}^{h_1 h_2 \times B}, i = 1,2,...,N, \tag{25}$$

where $\mathbf{z}_{i,l,j}$ denotes the jth vectorized patch in $\mathbf{T}_{i,l}, l = 1,...,L_1$. B is the number of blocks when using a block of size $h_1 \times h_2$ to slide each $\mathbf{T}_{i,l}, l = 1,...,L_1$, with overlap ratio R and given by

$$B = \left[1 + \left(m + k_1 - 1 - h_1 \right) / \text{stride1} \right] \cdot \left[1 + \left(n + k_2 - 1 - h_2 \right) / \text{stride2} \right], \tag{26}$$

where stride1 and stride2 are vertical and horizontal steps, respectively,

$$\text{stride1} = round\left(\left(1 - R \right) \cdot h_1 \right), \tag{27}$$

$$\text{stride2} = round\left(\left(1 - R \right) \cdot h_2 \right), \tag{28}$$

and *round* (.) means round off. As we can see from (26)-(28), the number of blocks B is increasing as the overlap ratio R is increasing.

For L_1 images, we concatenate $\mathbf{Z}_{i,l}$ to obtain a matrix

$$\mathbf{Z}_i = \left[\mathbf{Z}_{i,1} \quad \mathbf{Z}_{i,2} \quad \cdots \quad \mathbf{Z}_{i,B} \right] \in \mathbb{R}^{h_1 h_2 \times L_1 B}, i = 1,2,...,N, \tag{29}$$

We denote $\mathbf{Z}$ as

$$\mathbf{Z} = \left[\mathbf{Z}_{1,1} \quad \cdots \quad \mathbf{Z}_{1,B} \quad \cdots \quad \mathbf{Z}_{N,1} \quad \cdots \quad \mathbf{Z}_{N,B} \right] \in \mathbb{R}^{h_1 h_2 \times L_1 BN}. \tag{30}$$

Step 10: histogram.

We compute the histogram (with 2^{L_2} bins) of the decimal values in each column of $\mathbf{Z}_i$ and concatenate all the histograms into one vector and obtain

$$\mathbf{f}_i = \left[\text{Hist}(\mathbf{z}_{i,1,1}) \quad \cdots \quad \text{Hist}(\mathbf{z}_{i,1,B}) \quad \cdots\cdots \quad \text{Hist}(\mathbf{z}_{i,L_1,1}) \quad \cdots \quad \text{Hist}(\mathbf{z}_{i,L_1,B}) \right]^T \in \mathbb{R}^{(2^{L_2}) L_1 B}. \tag{31}$$

which is the "feature" of the input image $\mathbf{I}_i$ and Hist(.) denotes the histogram operation. We denote $\mathbf{f}$ as

$$\mathbf{f} = \left[\mathbf{f}_1 \quad \cdots \quad \mathbf{f}_N \right] \in \mathbb{R}^{(2^{L_2}) L_1 BN}. \tag{32}$$

The feature vector is then sent to a classifier, for example, support vector machine (SVM) [72], k-nearest neighbors algorithm (KNN) [73], etc.

2.4. The parameters of PCANet

The dimension of PCANet feature is related to the core parameters shown in Table 1. For a given dataset, m and n are fixed. In this paper, we always set $k_1=k_2=3$ since in this case the consumption of memory is tolerable for an ordinary computer (for example, 64 GB RAM). Note also that we set a constraint

$$h_2 = \lfloor nh_1 / m \rfloor, \tag{33}$$

which is a common choice in practice. After the above setting, there are four free parameters left: L_1, L_2, h_1, and R.

3. Energy Analysis and Energy Explanation of PCANet

In this section, we introduce the details of the proposed energy explanation approach method. We first present the motivation of the proposed approach, and then we describe the experiment methods and the used databases. The following experiments were implemented in Matlab programming language.

3.1. Motivations

CNNs are visualized and understood by using back-trace or inverted method to show the filters (or weights) that are learned by every layer [48, 52, 55]. The filters show much information since CNNs generally have many layers and the number of these filters are very large. Chan *et al*. [56] also visualize the filters of PCANet like in [48], [52], and [55]. However, PCANet does not have such large number of filters like CNNs, therefore, visualizing the filters only provides limited information about two filter layers (*Steps 3* and *6*) of PCANet. Furthermore, how to effectively visualize other implemental steps (*Steps 1, 2, 4, 5*, and *7-9*) of PCANet is still an open problem since these simple operations have a prominent impact on the performance of PCANet. For example, as depicted in [56], the performance of PCANet is degraded if we delete the simple mean-remove process.

On the one hand, PCA, also known as Karhunen-Loeve transform (KLT), is very popular in data compression domain since it has very good energy concentration capability, that is, few coefficients of KLT capture vast majority of energy of the original signal. On the other hand, Mallat and Bruna [44, 45] also prove and explain ScatNet from energy perspective. However, there are two main differences between PCANet and ScatNet [44, 45]: (1) the convolutional layer of PCANet is constructed by data-dependent PCA filter while the convolutional layer of ScatNet is constructed by data-free complex wavelet filter; (2) the nonlinearity of PCANet is binarization while the nonlinearity of ScatNet is modulus. The aforementioned two aspects lead to a question: can we explain every step of PCANet from an energy

perspective?

3.2. Experiment databases

In the following, we use five databases, whose Matlab formats are provided in [71] and [74], to analyze the energy change as well as the error rate change of PCANet: **1) Yale database** [67]. It contains 165 grayscale images (15 individuals, 11 images per individual), which are randomly divided into 30 training images and 135 testing images; **2) AR database** [68]**.** We use a non-occluded subset of AR database containing 700 images (50 male subjects, 14 images per subject), which are randomly divided into 200 training images and 500 testing images; **3) The CMU PIE face database** [69]. We use pose C27 (a frontal pose) subset of CMU PIE face database which has 3400 images (68 persons, 50 images per person), which are randomly divided into 1000 training images and 2400 testing images; **4) ORL database** [70]. It contains 400 grayscale images (40 individuals, 10 images per individual), which are randomly divided into 80 training images and 320 testing images. 5**) CIFAR-10 database** [71]. The original database contains 60000 color images (10 classes), including 50000 training images and 10000 test images. In our experiment, we randomly choose 3000 images for training and 1000 images for testing. Note that the size of all the images is 32×32 pixels. For the cross validation, we use the simplest hold-out validation due to the following two reasons: 1) some cases of the experiments are time and memory consuming; 2) the objective of the paper is not to achieve the lowest error rate but to establish the one-to-one correspondence of error rate e and the inverse of the logarithm of BlockEnergy g, and then find the parameters to achieve the relatively low error rate by the guidance of energy. Therefore, we need e and g are directly correspondent.

3.3. Experiment methods

In this section, we exploit the above-mentioned databases to analyze the PCANet by using energy method. We first introduce the definition of the energy of a two-dimensional image $\mathbf{I}(i, j)$ of size $m \times n$:

$$E(\mathbf{I}) = \sum_{i=1}^{m} \sum_{j=1}^{n} \mathbf{I}^2(i, j) . \tag{34}$$

Fig. 1 shows that we record 10 energies for PCANet. It is convenient for us to divide these energies into two parts: Energies 1-9 belong to the first part and Energy 10 belongs to the second part. The reason for this partitioning is that Energies 1-9 are not related to the block size $h_1 \times h_2$ and the overlap ratio R. The values that we recorded in the whole process of PCANet are shown in Table 2, which includes 10 energies and the error rate. Note that we do not take the

energy of the feature **f** in (32) into consideration, since the block-wise histogram is only the statistic (or occurrence frequency) of energy value and we consider that this process does not change the energy.

3.3.1 The analysis of the second part

In this subsection, we first introduce two metrics of the experiments. The first metric is the inverse of the logarithm of BlockEnergy $E(\mathbf{Z})$, shown in Table 2, that is

$$g = 1/\log_{10}\left(E(\mathbf{Z})\right). \tag{35}$$

The second metric is the error rate

$$e = \frac{\text{The number of false classified testing images}}{\text{The total number of testing images}}. \tag{36}$$

In the second part, there are 4 free parameters: h_1 (the number of rows of block), R (the overlap ratio), L_1 (the number of filters of the 1st stage), L_2 (the number of filters of the 2nd stage). Therefore, the aim of this subsection is to explore qualitatively the metric g and also the metric e with regards to the parameters h_1, R, L_1, and L_2.

1) How the g and the e qualitatively vary according to h_1, R, L_1, and L_2?

In this experiment, we use Yale database for analyzing the g and also the e in relation with h_1, R, L_1, L_2, where $h_1 \in \{1{:}1{:}32\}$, $R \in \{0{:}0.1{:}0.9\}$, and $L_1, L_2 \in \{1{:}1{:}9\}$. Note that $\{a{:}b{:}c\}$ means the set contains the values that vary from a to c with increment b. Each combination of h_1, L_1, L_2, and R has a e value or g value. Therefore, if we denote M as the total number of e or g, then, M=32×10×9×9=25920.

The results of the variations of g according to h_1, R, L_1, L_2 are shown in Fig. 2, whose vertical axis is $h_1 \in \{1{:}1{:}32\}$ and horizontal axis is related to R and L_2. Specifically, the horizontal axis can be divided into 9 blocks corresponding to $L_2 \in \{1{:}1{:}9\}$, each block can further be divided into 10 sub-blocks corresponding to $R \in \{0{:}0.1{:}0.9\}$, where each sub-block has the size of 32×1. Therefore, the range of horizontal axis value is from 1 to 90 (=10×9). Fig. 2(a) is in fact the concatenated version of 90 images. In Fig. 2, g is expressed by colors. The brown and the blue denote the values 1 and 0, respectively. The pure brown area appears in the figure in fact denotes that the algorithm cannot work in these cases, specifically, **the function of** "HashingHist" in the PCANet software can not deal with these cases, we manually set g=1. It does not matter, the pure brown areas are just used in Fig. 2 as separators of the results of various L_2. The similar results of e according to h_1, R, L_1, L_2 are shown in Fig. 3. From Figs. 2 and 3, we can see that:

a) *The impact of L_1 on g and e.* Both Fig. 2 and Fig. 3 contain 9 similar figures corresponding to $L_1 \in \{1:1:9\}$. If we fix L_2 and increase L_1, then, both *g* and *e* are gradually decreased. When $L_1 \geq 4$, the figures are flattened. The first three figures have notable changes, this phenomenon implies that the first few number of filters captures most of the energies of the original image, leading to the severe changes of *g* and *e*.

b) *The impact of L_2 on g and e*. As the value of L_2 increases, the first five figures corresponding to $L_2 \in \{1:1:5\}$ change a lot, but when $L_2 \geq 6$, the left four figures only make little changes. Therefore, we can think that when $L_2 = 6$, both *g* and *e* are stable.

c) *The impact of R on g and e*. There are some differences of the changes of *g* and *e* according to *R*. From Fig. 2, we can see that *g* is gradually decreased as the value of *R* increases. However, from Fig. 3, the probability of lower error rate *e* is increased as the value of *R* increases from 0 to 0.9 with interval of 0.1. Nonetheless, the appropriate values of *R* in fact belong to {0:0.1:0.6}, due to the following two reasons: Firstly, from the experimental aspect, when $R \geq 0.7$, it may encounter the cases where PCANet can not work; When $R \geq 0.7$, the result is also good if it does not encounter the cases where PCANet can not work, but both the computational and the memory complexities are very high from experiment aspect since they lead to too much overlap. Let us take Yale database for example, setting $k_1=k_2=3$, $L_1=L_2=8$, $h_1=h_2=8$, Table 3 shows the accuracy, time consumption, and dimension of features when *R* varies from 0 to 0.9. Secondly, from the theory or explanation aspect, the overlap ratio *R* has a similar role with the eigenvector in PCA filtering as shown in Appendix. In the case of realizing dimension reduction by PCA, we want to use as few as possible eigenvectors while keeping enough useful features of original image. Similarly, we want to use as small as possible overlap ratio *R*.

d) *The impact of h_1 on g and e*.

As we can see, when h_1 is higher than a critical value $(m+k_1-1)/2+10R$, each block has an obvious trapezoidal area, where the values of *g* and *e* are evidently higher than other parts of the block. The reason is that the block sliding process (*Step 9*) leads to "great reduction in energy" when $h_1 > (m+k_1-1)/2+10R$. Why this phenomenon appears? Let us take $R=0$ as an example, in this case, the critical value $(m+k_1-1)/2+10R=(32+3-1)/2+10\times0=17$. Figs. 4 (*a*) and (*b*) show the case of block sliding process of $h_1=17$ and $h_1=18$, respectively. From Fig. 4 (*a*), the image of 34×34 becomes an image of 4×289 by block sliding process with block of 17×17. In this case, all the information (or energy) of the image

is used through 3 times of block sliding process. However, as we can see from Fig. 4 (*b*), the image of 34×34 becomes an image of 1×324 by block sliding process with block of 18×18. Note that both the right side and the bottom side of the 18×18 block are not enough for a new block sliding process. In this case, we only use the information (or energy) of 18×18 block on the upper left corner, other information (or energy) of the image is not used. That is to say, the trapezoidal area is caused by "not making full use of energy". Therefore, the appropriate choice of the number of rows of block is $h_1 \leq (m+k_1-1)/2+10R$ since it can avoid the trapezoidal area.

In total, we can see the following things:

i) The changes of g and e have similar overall consistent trends, for example, the values of g and e are gradually decreased as the value of L_1 and L_2 increase.

ii) The changes of g are relatively smooth, while the changes of e seem more varied than that of g. Furthermore, e is not simply directly proportional to g.

2) How the e varies quantitatively according to g ?

In the following, we use the Curve Fitting Tool of Matlab to further investigate the correlation between e and g. We fit the function $e = f(g)$, by using the linear model Poly1 and the nonlinear model Poly3 in Matlab with 95% confidence bounds, that is, we used $e = p_1 g + p_2$, and $e = p_3 g^3 + p_4 g^2 + p_5 g + p_6$, where p_i, $i = 1,2,\ldots,6$, are the coefficients to fit, to find the relationship of e and g, respectively. The curve fitting results of five datasets are shown in Fig. 5 and the quantitative results are shown in Table 4. The criterions include:

a) The sum of error squares (SSE), sum of regression squares (SSR), and total sum of squares (SST) are defined respectively as

$$SSE = \sum_{i=1}^{M} (e_i - f(g_i))^2 , \tag{37}$$

$$SSR = \sum_{i=1}^{M} (f(g_i) - \bar{e})^2 , \tag{38}$$

$$SST = SSE + SSR = \sum_{i=1}^{M} (e_i - \bar{e})^2 , \tag{39}$$

where $\bar{e} = \frac{1}{M}\sum_{i=1}^{M} e_i$, and i is the index of the number of e or g, and M is the total number of e or g. In our experiment, M=32×10×9×9=25920.

b) Coefficient of determination or R-square is defined as

$$r^2 = 1 - \frac{SSE}{SST}, \tag{40}$$

which is a number that indicates how well data fit a statistical model, for example, a curve.

c) Root mean squared error (RMSE) is defined as

$$RMSE = \sqrt{\frac{\sum_{i=1}^{N}(e_i - f(g_i))^2}{N}}. \tag{41}$$

As we can see from Table 4, the R-square of the data of Yale database by using linear model Poly1 is 0.6104, which means 61.04% of the variance in the response variable can be explained by the explanatory variables. Therefore, e and g are fairly linearly correlated. As we mentioned above that the changes of g and e have similar overall consistent trends but the changes of e seem more varied than that of g. Can we use a little more complicated model for describing the correlation between e and g? We then use a nonlinear polynomial function of degree 3 (Poly3) to model the relationships of e and g. The R-square of the data of Yale database by using model Poly3 is 0.6288, which means 62.88% of the variance in the response variable can be explained by the explanatory variables. The remaining 37.12% can be attributed to unknown, lurking variables or inherent variability. Therefore, e and g are fairly non-linearly correlated. We also give the curve fitting results for the data of five databases (Yale, AR, CMU PIE, ORL, CIFAR-10) in Table 4. Similar conclusion can be obtained for the other databases. In fact, if we cancel the constraint in (33) and do the similar experiment on Yale database, the R-square of the data of Yale database by using Poly3 increases further to 0.7637, which is even larger than 0.6288 that has the constraint in (33).

3) *How to explain the block sliding process*?

We can in fact explain this process as an "overlap filtering", which is a term that we proposed in this paper to explain and better understand the sliding process, including the patch sliding process and the block sliding process. The idea of "overlap filtering" is in fact from the PCA filter. The comparison and the connection of "overlap filtering" and PCA filter are given in Appendix and also in Table 5.

3.3.2 The analysis of the first part

In this subsection, we will analyze the changes of Energies 1-9 of the first part of PCANet shown in Fig. 1. Since the first part is not related to h_1, h_2, and R, so in the experiment of this section, we simply set the parameters $h_1 = h_2 = 8$, and R= 0.5, due to the following three reasons: (1) they are near one of the recommended parameters h_1 =8, h_2 = 6, and R= 0.5 in PCANet [56]; (2) they have the moderate computational complexity and memory complexity; (3) they satisfy the constraint $h_2 = \lfloor nh_1 / m \rfloor$ in (33) in the analysis of the second part. Let us take Yale dataset as an example, Fig. 6 shows the energy values of every stage of the first part of PCANet versus the ith energy. The results of 9 filters, corresponding to $L_1 \in \{1{:}1{:}9\}$, are shown in different colors. For example, the lowest line is the result that we choose only the largest eigenvector corresponding to L_1=1. The second lowest line is the result that we choose the 2 largest eigenvectors corresponding to L_1=2, and so on. Note that the vertical axis is shown in logarithmic coordinate. From Fig. 6, for all the 9 filters, we can easily see that the energy changes are as follows

$$\begin{aligned}
&\textbf{TrainEnergy} \xrightarrow[\text{Step 1}]{+} \textbf{PatchEnergy}1 \\
&\xrightarrow[\text{Step 2}]{-} \textbf{PatchEnergyRed}1 \\
&\xrightarrow[\text{Step 3}]{+ \text{ or } -} \textbf{PCAEnergy}1 \xrightarrow[\text{Step 4}]{+} \textbf{PatchEnergy}2 \\
&\xrightarrow[\text{Step 5}]{\mathbf{0}} \textbf{PatchEnergyRed}2 \\
&\xrightarrow[\text{Step 6}]{+ \text{ or } -} \textbf{PCAEnergy}2 \xrightarrow[\text{Step 7}]{-} \textbf{BinaryEnergy} \\
&\xrightarrow[\text{Step 8}]{+} \textbf{WeightSumEnergy},
\end{aligned} \tag{42}$$

where the arrow means that the energy values change from the left-hand side to the right-hand side. “+”, “–”, “0” above the arrow denote the energy increase, decrease, and equal process, respectively. Steps 1-8 below the arrow correspond to the eight steps of Fig. 1.

From (42), we can see that:

1) For Steps 1 and 4, both of them are energy increasing processes, which can be easily understood since these two steps perform the overlapping patch sliding process. However, how can we explain the patch sliding process? In fact, the patch sliding process is a special case of block sliding process with the overlap ratio R=0.9 shown in **the second part**.

2) For the Steps 2 and 5, both of them are mean removing processes. Step 2 is energy decreasing process, which is reasonable since the mean removing leads to the reduction of image energy. **However, it is strange that Step 5 keeps**

the energy. Therefore, we think this step may not be needed in the construction of PCANet. We then perform some experiments on four databases to verify our inference. We compute the differences of error rates of PCANet with mean remove Step 5 and that of without Step 5 for all the parameter setting of $h_1 \in \{1:1:32\}$, $R \in \{0:0.1:0.9\}$, and L_1, $L_2 \in \{1:1:9\}$. The mean of differences of error rates for Yale database, AR database, CMU PIE database, and ORL database are 1.1762×10^{-6}, 1.5878×10^{-7}, -1.4886×10^{-7}, -4.9619×10^{-7}, respectively, all of which are very small. **Therefore, when taking the computational complexity into consideration, we recommend to not use the mean remove process of Step 5.**

3) For the Steps 3 and 6, both of them are PCA processes. Both Step 3 and Step 6 are energy increasing processes except the case of 1 filter, but the energy change is very small. Table 6 shows the energy of each of the 9 filters (the 1st PCA), $h_1=h_2=8$, $R=0.5$, $L_2=1$, and L_1 varies from 1 to 9, and the energy of every filter (the 2nd PCA), $h_1=h_2=8$, $R=0.5$, $L_1=8$, and L_2 varies from 1 to 9. Table 7 shows the error rate corresponding to L_1, $L_2 \in \{1:1:9\}$ when $h_1=h_2=8$, $R=0.5$. From the two Tables, we can see that the cumulative percentage of eigenvalue can be a guideline for the choice of L_1 and L_2, for example, the error rate of Yale database is low when the cumulative percentage of eigenvalue is larger than 99.7%, which corresponds to $L_1=8$ and $L_2=8$. Note that $L_1=L_2=8$ is just one of the parameter settings recommended by Chan's paper [56].

4) For the Steps 7 and 8, which cause the sharpest energy changes of PCANet. It is also reasonable since the binarization operation is a very powerful quantization process (nonlinear processing), which loses much energy. Meanwhile, the weighted and summed step is a very powerful energy increasing step. It is interesting to see from Fig. 6 that the energy in Step 8 gradually increases when L_2 varies from 1 to 9. Let's focus on the two horizontal dashed lines: the first one denotes the **MaxEnergyLinear (**maximum energy of linear layer of PCANet**)** including either **PatchEnergy2** or **PCAEnergy2**, and the second one denotes the **TrainEnergy**. We can see from Fig. 6 and Table 7:

a) When **WeightSumEnergy**<**TrainEnergy**, corresponding to Fig. 6 (*a*)-(*e*), the error rate is gradually decreased when $L_1 \in \{1:1:9\}$ and $L_2 \in \{1:1:5\}$.

b) When **TrainEnergy** < **WeightSumEnergy** ≤ **MaxEnergyLinear**, corresponding to Fig. 6 (*f*)-(*h*), the error rate is flattened when $L_1 \in \{1:1:9\}$ and $L_2 \in \{6:1:8\}$.

c) When **WeightSumEnergy>MaxEnergyLinear**, corresponding to Fig. 6 (*i*), the error rate is increased when $L_1 \in \{1:1:9\}$ and $L_2=9$. In this case, we think that the **WeightSumEnergy** includes "pseudo energy" so that the **WeightSumEnergy** is even larger than the maximum energy of linear layer of PCANet.

Note that the above experiments performed in other four databases (AR database, CMU PIE face database, ORL database, CIFAR-10 database), the results of which correspond to the Fig. 2, Fig. 3, Fig. 5, and Tables 5-7 of YALE database are provided in the supplement document due to the limited space. The results of other three databases are similar to that of Yale database.

Therefore, we can conclude from the aforementioned analysis:

1) For the linear process of PCANet (Steps 1 to 6), repeated use of the combination of patch sliding process, mean removing process, and PCA increases the energy and seems beneficial for the recognition performance of PCANet. It may explain that two-layer PCANet can generally obtain better recognition performance than one-layer PCANet.
2) For the nonlinear process of PCANet (Steps 7 and 8), the choice of the value of L_2 is very important. When we choose a proper L_2 value, which makes **WeightSumEnergy** comparable to the **TrainEnergy** (like Fig. 6 (*f*))**,** in this case, PCANet can generally lead to good results.
3) We can eliminate the mean removing process of Step 5 when taking the computational complexity into consideration since there is no energy changes in this step and the recognition performances of PCANet with or without Step 5 are very similar.
4) The changes of *e* (error rate) seem more varied than that of *g* (the inverse of the logarithm of **BlockEnergy**), however, correlations between *e* and *g* are fairly strongly non-linear as underlined when using the model Poly3 in Matlab. Therefore, **BlockEnergy** may be seen as a wind arrow for the error rate of PCANet.

4. Discussion

This section discusses some issues related to the proposed energy explanation method.

Parameter settings of k_1 and k_2. In this paper, we always set $k_1=k_2=3$ due to the following two reasons:

(1) The parameters setting of $k_1=k_2=3$ is a representative choice since filter kernels with the size 3×3 are the most common choices in the design of CNNs, for example, VGGNet [16], ResNet [17], etc.

(2) In this case, we have $1\le L_1\le 9$ and $1\le L_2\le 9$, that is to say, the number of outputs of PCANet is at most 81 times of that of input after the *Step 6*. The consumption of memory is tolerable for an ordinary computer (for example, 64 GB

RAM). Let us take Yale dataset for an example (m=n=32), if we set L_1=L_2=9, h_1=h_2=6, R=0.9, the dimension of the resulting PCANet feature after *Step 10* is 3875328, which is tolerable for SVM and KNN classifiers. However, if we set k_1=k_2=5, the most time and memory consumption case is L_1= L_2=25, that is to say, the number of outputs of PCANet is 625 times of that of input after the *Step 6*. Let us still take Yale dataset for an example (m=n=32), if we set L_1=L_2=25, h_1=h_2=6, R=0.9, *Step 10* (HashingHist function) will apply a memory for the matrix of size 33554432×961 (240.3GB), which is unbearable for Matlab and also a very challenge dimension for SVM and KNN classifiers. As a further direction, we will try to extend to other parameter settings (k_1=k_2=5, k_1=k_2=7, etc.) when higher performance machines will be available.

The impact of classifier. Besides SVM, we also give the results of KNN classifier of three datasets (Yale dataset, AR dataset, ORL dataset) in the supplement document. Results show that the error rates of PCANet by using the SVM and the KNN classifiers can be nearly fitted by linear function.

The size of dataset. The number of images in the database affects the speed and memory consumption of PCANet. Specifically, when the number of images increases, the covariance matrix computation in the PCA filter becomes slow and the training of SVM and KNN classifiers also becomes slow; meanwhile, it needs training more parameters and thus more memory consumption when training SVM and KNN classifiers. Therefore, the number of images is also not allowed to be big (for example, less than 4000 images for a color image database) in order to ensure the SVM and KNN classifications.

The impact of cross validation. Besides the simplest hold-out validation (or 2-fold cross validation) in the above experiments, we also do the 5-fold cross validation on Yale dataset, we find the curve fitting results are slightly worse than that of the hold-out validation. The reason is that both the error rate and the energy are the average values of 5 experiments, however, the relation of the average values of error rate is in fact not actually corresponding to the average of values of the energy. Therefore, 5-fold cross validation can make the error rate of a dataset more reasonable, but it is not suitable for our case since our method needs the direct correspondences of the energy and the error rate but not their average values.

5. Conclusions

In this paper, an energy method is proposed to visualize, explain and understand every step of PCANet. The paper shows that the error rate of PCANet is qualitatively correlated with the inverse of the logarithm of **BlockEnergy**, and

then their relations are further quantified by using curve fitting methods. The role and the explanation of every step of PCANet have been investigated, for example, the patch sliding process and the block sliding process are explained by "overlap filtering". The proposed energy explanation approach could be used as a testing method for checking if every step of the constructed networks is necessary. For example, we find that the second mean remove step is not needed in the construction of PCANet since the energy is not changed. The proposed energy explanation approach can provide more information than the filter visualization method shown in [56]. Furthermore, the proposed energy explanation approach can be extended to other PCANet-based networks [57-66].

Appendix Comparisons of PCA Filter and Overlap filtering

	PCA Filter	Overlap filtering
Objective	Minimize the reconstruction error in Frobenius norm as $\min_{\mathbf{U}\in\mathbb{R}^{k_1k_2\times L_1}} \left\|\bar{\mathbf{X}}-\mathbf{U}\mathbf{U}^T\bar{\mathbf{X}}\right\|_F^2$, s.t. $\mathbf{U}^T\mathbf{U}=\mathbf{D}_{L_1}$, (A.1) where $\mathbf{D}_L$ is an identity matrix of size $L\times L$, the superscript T denotes transposition, and $\bar{\mathbf{X}}\in\mathbb{R}^{k_1k_2\times Nmn}$.	How to explain the sliding process, including the patch sliding process and the block sliding process? How to choose an appropriate overlap ratio R?
Solve	**Eigenvalue decomposition method** Eq. (A.1) can be solved by eigenvalue decomposition method $\mathbf{C}_1=\mathbf{U}\mathbf{\Lambda}_1\mathbf{U}^T$, (A.2) where $\mathbf{C}_1$ is a covariance matrix given by $\mathbf{C}_1=\frac{1}{Nmn}\bar{\mathbf{X}}\bar{\mathbf{X}}^T\in\mathbb{R}^{k_1k_2\times k_1k_2}$, (A.3) and $\mathbf{\Lambda}_1$ is a diagonal matrix composed of the first L_1 largest eigenvalues of $\mathbf{C}_1$, $\mathbf{\Lambda}_1=diag\left[\lambda_1^I \quad \lambda_2^I \quad \cdots \quad \lambda_{L_1}^I\right]$, (A.4) where $\lambda_1^I\geq\lambda_2^I\geq\cdots\geq\lambda_{L_1}^I$, and the superscript of capital Roman number I denotes the first stage, and $\mathbf{U}$ is the matrix composed of the first L_1 principal eigenvectors $\mathbf{U}=\left[\mathbf{u}_1 \quad \mathbf{u}_2 \quad \cdots \quad \mathbf{u}_{L_1}\right]\in\mathbb{R}^{k_1k_2\times L_1}$. (A.5)	**Explain the sliding process as an "overlap filtering"** 1) Suppose we use a block $h_1\times\lfloor nh_1/m\rfloor$, $1\leq h_1\leq m$, to slide an image, we can get at most 10 images. The energy of each image has a similar effect with the eigenvalue in PCA filtering. The overlap ratio R=0,0.1,0.2,...,0.9, corresponds to the 1st, 2nd, 3rd, ..., 10th eigenvectors in PCA filtering. 2) Rearrange the energy of the 10 images, that is, sort the energy values in the descending order. This is shown in the 3th row of Table 5.
How to choose the parameter?	**How to choose the number of filters L?** **Cumulative energy method** 1) Compute the cumulative energy content g as $g_j=\sum_{i=1}^{j}\lambda_i^I, j=1,...,k_1k_2$. 2) Use the vector $\mathbf{g}$ as a guide in choosing an appropriate value for L. The goal is to choose a value of L as small as possible while achieving a reasonably high value of g on a percentage basis, for example, the cumulative energy g is above a certain threshold, like 90 percent, that is, $g_L/g_{k_1k_2}\geq 0.9$.	**How to choose the overlap ratio R?** **Cumulative energy method** We show the ratio of energy in the 5th row. As shown in **Section 3.3.1**, $R\in\{0{:}0.1{:}0.6\}$ is appropriate for PCANet. We can see from Table 5, the energy we keep is about 95.75% when R=0.6, which seems the point that comprises the training error and the generalized error. Therefore, the energy can be used as a guidance for the choice of an appropriate overlap ratio R.

Acknowledgement

This work was supported by the National Key R&D Program of China (2017YFC0107900), by the National Natural Science Foundation of China (Nos. 61271312, 61201344, 61773117, 61401085, 31571001, 31640028, 31400842, 61572258, 11301074), by the Natural Science Foundation of Jiangsu Province under Grant BK20150650, by the Qing

Lan Project and the '333' project (BRA2015288), and by the Short-term Recruitment Program of Foreign Experts (WQ20163200398). The authors are also grateful to the anonymous reviewers for their constructive comments and suggestions to greatly improve the quality of this work and the clarity of the presentation.

References

[1] G. E. Hinton, S. Osindero, Y.W. Teh, A fast learning algorithm for deep belief nets, *Neural Comput.*, 18(2006) 1527-1554.
[2] G. E. Hinton, R. R. Salakhutdinov, Reducing the dimensionality of data with neural networks, *Science*, 313(2007) 504-507.
[3] Y. Bengio, P. Lamblin, D. Popovici, H. Larochelle, Greedy layer-wise training of deep networks, in *Proc. NIPS*, (2007) 153-160.
[4] H. Lee, R. Grosse, R. Ranganath, A.Y. Ng, Convolutional deep belief networks for scalable unsupervised learning of hierarchical representations, in *Proc. ICML*, (2009) 609-616.
[5] P. Vincent, H. Larochelle, Y. Bengio, P.A. Manzagol, Extracting and composing robust features with denoising autoencoders, in *Proc. ICML*, (2008) 1096-1103.
[6] Y. LeCun, Y. Bengio, G. E. Hinton, Deep learning, *Nature*, 521(2015) 436-444.
[7] Y. Bengio, Learning deep architectures for AI, *Foundat. and Trends Mach. Learn.*, 2(2009) 1-127.
[8] L. Deng, D. Yu, Deep Learning: Methods and Applications, *Foundations and Trends® in Signal Processing*, 7(2013) 197-387.
[9] Y. Bengio, A. Courville, P. Vincent, Representation learning: A review and new perspectives, *IEEE Trans. Pattern Anal. Mach. Intell.*, 35(2013) 1798-1828.
[10] J. Schmidhuber, Deep learning in neural networks: An overview, *Neural Networks*, 61(2015) 85-117.
[11] Y. LeCun, B. Boser, J. S. Denker, D. Henderson, R. E. Howard, W. Hubbard, L. D. Jackel, Backpropagation applied to handwritten zip code recognition, *Neural Comput.*, 1(1989) 541-551.
[12] Y. LeCun, L. Bottou, Y. Bengio, P. Haffner, Gradient-based learning applied to document recognition, *Proc. IEEE*, 86(1998) 2278-2324.
[13] O. Russakovsky, J. Deng, H. Su, J. Krause, S. Satheesh, S. Ma, Z. Huang, A. Karpathy, A. Khosla, M. Bernstein, A. C. Berg, F.F. Li, ImageNet large scale visual recognition challenge, *Int. J. Comput. Vis.*, 115(2015) 211-252.
[14] A. Krizhevsky, I. Sutskever, G. E. Hinton, ImageNet classification with deep convolutional neural network, in *Proc. NIPS*, (2012) 1097-1105.
[15] C. Szegedy, W. Liu, Y. Jia, P. Sermanet, S. Reed, D. Anguelov, D. Erhan, V. Vanhoucke, A. Rabinovich, Going deeper with convolutions, in *Proc. IEEE Conf. CVPR*, (2015) 1-9.
[16] K. Simonyan, A. Zisserman, Very deep convolutional networks for large-scale image recognition, http://arxiv.org/abs/1409.1556, 2014.
[17] K. He, X. Zhang, S. Ren, J. Sun, Deep residual learning for image recognition, http://arxiv.org/abs/1512.03385, 2015.
[18] E. Learned-Miller, G. Huang, A. RoyChowdhury, H. Li, G. Hua, Labeled faces in the wild: A survey, http://people.cs.umass.edu/~elm/papers/LFW_survey.pdf, 2015.
[19] Y. Sun, D. Liang, X. Wang, X. Tang, DeepID3: Face recognition with very deep neural networks, http://arxiv.org/abs/1502.00873, 2015.
[20] F. Schroff, D. Kalenichenko, J. Philbin, FaceNet: A unified embedding for face recognition and clustering, Computer Vision and Pattern Recognition(CVPR), (IEEE2015), pp. 815-823.
[21] D. Ciresan, U. Meier, J. Schmidhuber, Multi-column deep neural networks for image classification, Computer Vision and Pattern Recognition(*CVPR)*, (IEEE2012), pp. 3642-3649.
[22] S. Zhang, J. Wang, X. Tao, Y. Gong, N. Zheng, Constructing deep sparse coding network for image classification, Pattern Recognition, 64(2017) 130-140.
[23] C. Zu, Z. Wang, D. Zhang, P. Liang, Y. Shi, D. Shen, G. Wu, Robust multi-atlas label propagation by deep sparse representation, Pattern Recognition 63(2017) 511-517.

[24] E. Ohn-Bar, M. M. Trivedi, Multi-scale volumes for deep object detection and localization, Pattern Recognition 61(2017) 557-572.
[25] A. T. Lopes, E. de Aguiar, A. F. DeSouza, T. Oliveira-Santos, Facial expression recognition with Convolutional Neural Networks: Coping with few data and the training sample order, Pattern Recognition, 61(2017) 610-628.
[26] X. Q. Zhou, B. T. Hu, Q. C. Chen, X. L. Wang, Recurrent convolutional neural network for answer selection in community question answering, Neurocomputing 274 (2018) 8-18.
[27] Y. X. Chen, G, Tao, H. M. Ren, X. Y. Lin, L. M. Zhang, Accurate seat belt detection in road surveillance images based on CNN and SVM, Neurocomputing 274 (2018) 80-87.
[28] W. B. Liu, Z. D. Wang, X. H. Liu, N. Y. Zeng, Y, R, Liu, F. A. Alsaadi, A survey of deep neural network architectures and their applications, Neurocomputing 234 (2017) 11-26.
[29] S. Q. Yu, S. Jia, C. Y. Xu, Convolutional neural networks for hyperspectral image classification, Neurocomputing 219 (2017) 88-98.
[30] A. Qayyum, S. M. Anwar, M, Awais, M. Majid, Medical image retrieval using deep convolutional neural network, Neurocomputing 266 (2017) 8-20.
[31] P. Barros, G. I. Parisi, G. Weber, S. Wermter, Emotion-modulated attention improves expression recognition: A deep learning model, Neurocomputing, 2017, pp. 104-114.
[32] A. B. Patel, T. Nguyen, R.G. Baraniuk, A probabilistic theory of deep learning, http://arxiv.org/abs/1504.00641, 2015.
[33] P. Mehta, D. J. Schwab, An exact mapping between the variational renormalization group and deep learning, http://arxiv.org/abs/1410.3831, 2014.
[34] L. P. Kadanov, *Statistical Physics: Statics, Dynamics and Renormalization*. World Scientific, Singapore, 2000.
[35] N. Tishb, N. Zaslavsky, Deep learning and the information bottleneck principle, http://arxiv.org/abs/1503.02406, 2015.
[36] G.V. Steeg, A. Galstyan, The information sieve, http://arxiv.org/abs/1507.02284.
[37] O. Sigaud, A. Droniou, Towards deep developmental learning, *IEEE Trans. Auton. Mental Develop.*, doi: 10.1109/TAMD.2015.2496248.
[38] N. Lei, K. Su, L. Cui, S. -T. Yau, D. X. F. Gu, A geometric view of optimal transportation and generative model, http://arxiv.org/abs/1710.05488, 2017.
[39] X. Dong, J. S. Wu, L. Zhou, How deep learning works — The geometry of deep learning, http://arxiv.org/abs/1710.10784, 2017.
[40] A. Paul, S. Venkatasubramanian, Why does unsupervised deep learning work?-A perspective from group theory, http://arxiv.org/abs/1412.6621, 2015.
[41] U.Shaham, A.Cloninger, R. Coifman, Provable approximation properties for deep neural networks, http://arxiv.org/abs/1509.07385, 2015.
[42] F. Anselmi, L. Rosasco, T. Poggio, On invariance and selectivity in representation learning., http://arxiv.org/abs/1503.05938, 2015.
[43] F. Anselmi, J. Z. Leibo, L. Rosasco, J. Mutch, A. Tacchetti, T. Poggio, Unsupervised learning of invariant representations in hierarchical architectures, http://arxiv.org/abs/1311.4158, 2013.
[44] S. Mallat, Group invariant scattering, *Commun. Pure Appl. Math.*, 65(2012) 1331-1398.
[45] J. Bruna, S. Mallat, Invariant scattering convolution networks, *IEEE Trans. Pattern Anal. Mach. Intell.*, 35(2013), 1872-1886.
[46] T. Wiatowski, H. Bolcskei, Deep convolutional neural networks based on semi-discrete frames, in *Proc. IEEE ISIT*, (2015), pp. 1212-1216.
[47] J. Bruna, S. Chintala, Y. LeCun, S. Piantino, A. Szlam, M. Tygert, A theoretical argument for complex-valued convolutional networks, http://arxiv.org/abs/1503.03438, 2015.
[48] D. Erhan, Y. Bengio, A. Courville, P. Vincent, Visualizing higher-layer features of a deep network, Technical Report 1341, University of Montreal, 2009.
[49] H. Larochelle, D. Erhan, A. Courville, J. Bergstra, Y. Bengio, An empirical evaluation of deep architectures on problems with many factors of variation, in *Proc. ICML*, (2007), pp. 473-480.
[50] I.J. Goodfellow, Q.V. Le, A.M. Saxe, H. Lee, A.Y. Ng, Measuring invariances in deep networks, in *Proc. NIPS*, (2009), pp. 646-654.
[51] C. Szegedy, W. Zaremba, I. Sutskever, J. Bruna, D. Erhan, I. Goodfellow, R. Fergus, Intriguing properties of neural networks, *Computer Science*, (2014) 1-10.
[52] M.D. Zeiler, R. Fergus, Visualizing and understanding convolutional networks, in *ECCV*, 2014.

[53] K. Simonyan, A. Vedaldi, A. Zisserman, Deep inside convolutional networks: Visualising image classification models and saliency maps, in *Proc. ICLR*, 2014.
[54] R. Girshick, J. Donahue, T. Darrell, J. Malik, Rich feature hierarchies for accurate object detection and semantic segmentation, Computer Vision and Pattern Recognition (CVPR), 2014 IEEE Conference on, (IEEE2014).
[55] A. Mahendran, A. Vedaldi, Understanding deep image representations by inverting them, Computer Vision and Pattern Recognition (CVPR), 2014 IEEE Conference on, (IEEE2015), pp.5188-5196.
[56] T.-H. Chan, K. Jia, S. Gao, J. Lu, Z. Zeng, Y. Ma, PCANet: A simple deep learning baseline for image classification?, *IEEE Trans. Image Process.*, 24(2015) 5017-5032.
[57] Y. Gan, T. Yang, C. He, A deep graph embedding network model for face recognition, in *Proc. IEEE ICSP*, (2014), pp. 1268-1271.
[58] D. Wang, X. Tan, Unsupervised feature learning with C-SVDDNet, Pattern Recognition, 60 (2016) 473-485.
[59] Z. Feng, L. Jin, D. Tao, S. Huang, DLANet: A manifold-learning-based discriminative feature learning network for scene classification, *Neurocomputing*, 157(2015) 11-21.
[60] C. J. Ng, A. B. J. Teoh, DCTNet: A simple learning-free approach for face recognition, Proceedings of APSIPA Annual Summit and Conference, (2015), pp. 761-768.
[61] Y. Gan, J. Liu, J. Dong, G. Zhong, A PCA-based convolutional network, http://arxiv.org/abs/1505.03703, 2015
[62] Y. Zhao, R. Wang, W. Wang, W. Gao, Multi-level modified finite radon transform network for image upsampling, *IEEE Trans. Circuits Syst. Video Technol.*, 26(2015) 2189-2199.
[63] Z. Lei, D. Yi, S. Li, Learning stacked image descriptor for face recognition, *IEEE Trans. Circuits Syst. Video Technol.*, 26(2016) 1685-1696.
[64] S.Z. Li, B. Yu, W. Wu, S.Z. Su, R.R. Ji, Feature learning based on SAE-PCA network for human gesture recognition in RGBD images, *Neurocomputing*, 151(2015) 565-573.
[65] R. Zeng, J.S. Wu, Z.H. Shao, Y. Chen, B.J. Chen, L. Senhadji, H.Z. Shu, Color image classification via quaternion principal component analysis network, *Neurocomputing*, 216(2016) 416-428.
[66] J. S. Wu, S. J. Qiu, R. Zeng, Y.Y. Kong, L. Senhadji, H.Z. Shu. Multilinear principal component analysis network for tensor object classification. *IEEE Access*, 5 (2017) 3322-3331.
[67] Yale University, Yale Database, http://vision.ucsd.edu/content/yale-face-database.
[68] A.M. Martinez, R. Benavente, The AR face database, CVC Technical Report, 1998, http://www2.ece.ohio-state.edu/~aleix/ARdatabase.html.
[69] T. Sim, S. Baker, M. Bsat, The CMU pose, illumination, and expression (PIE) database, *Proc. International Conference on Automatic Face and Gesture Recognition*, 2002, http://www.multipie.org.
[70] Cambridge University Computer Laboratory, ORL datasets. http://www.cl.cam.ac.uk/research/dtg/attarchive/facedatabase.html
[71] A. Krizhevsky, Learning multiple layers of features from tiny images, *Technique Report*, 2009, 1-58.
[72] R.E. Fan, K.W. Chang, C.J. Hsieh, et al., LIBLINEAR: A library for large linear classification, *The Journal of Machine Learning Research*, 9 (2008) 1871-1874.
[73] N. S. Altman, An introduction to kernel and nearest-neighbor nonparametric regression. *The American Statistician*, 46 (1992) 175-185.
[74] D. Cai, X. He, J. Han, H. J. Zhang, Orthogonal laplacianfaces for face recognition, *IEEE Trans. Image Process.*, 15(2006), 3608-3614.

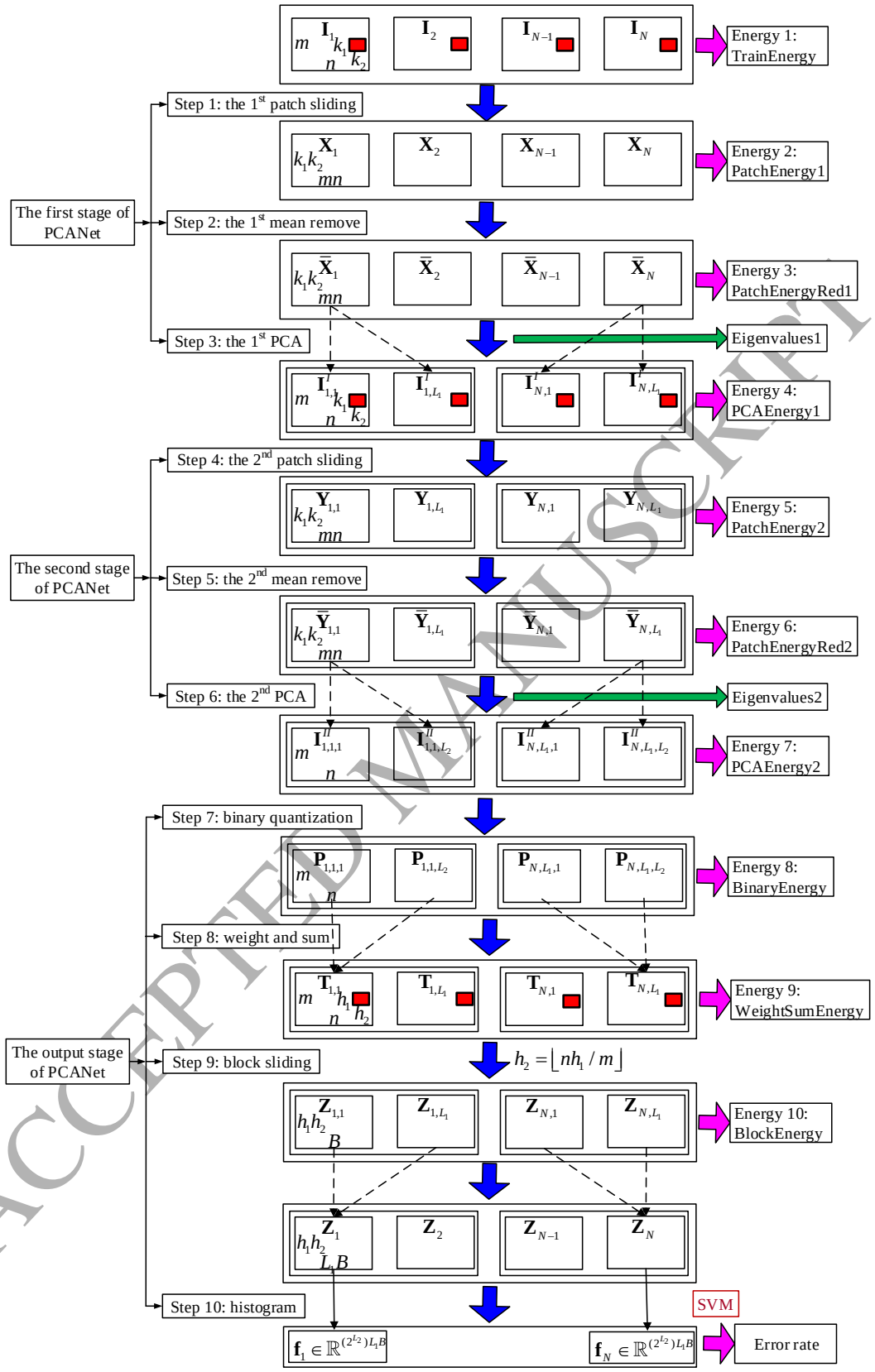

Fig. 1. The block diagram of PCANet

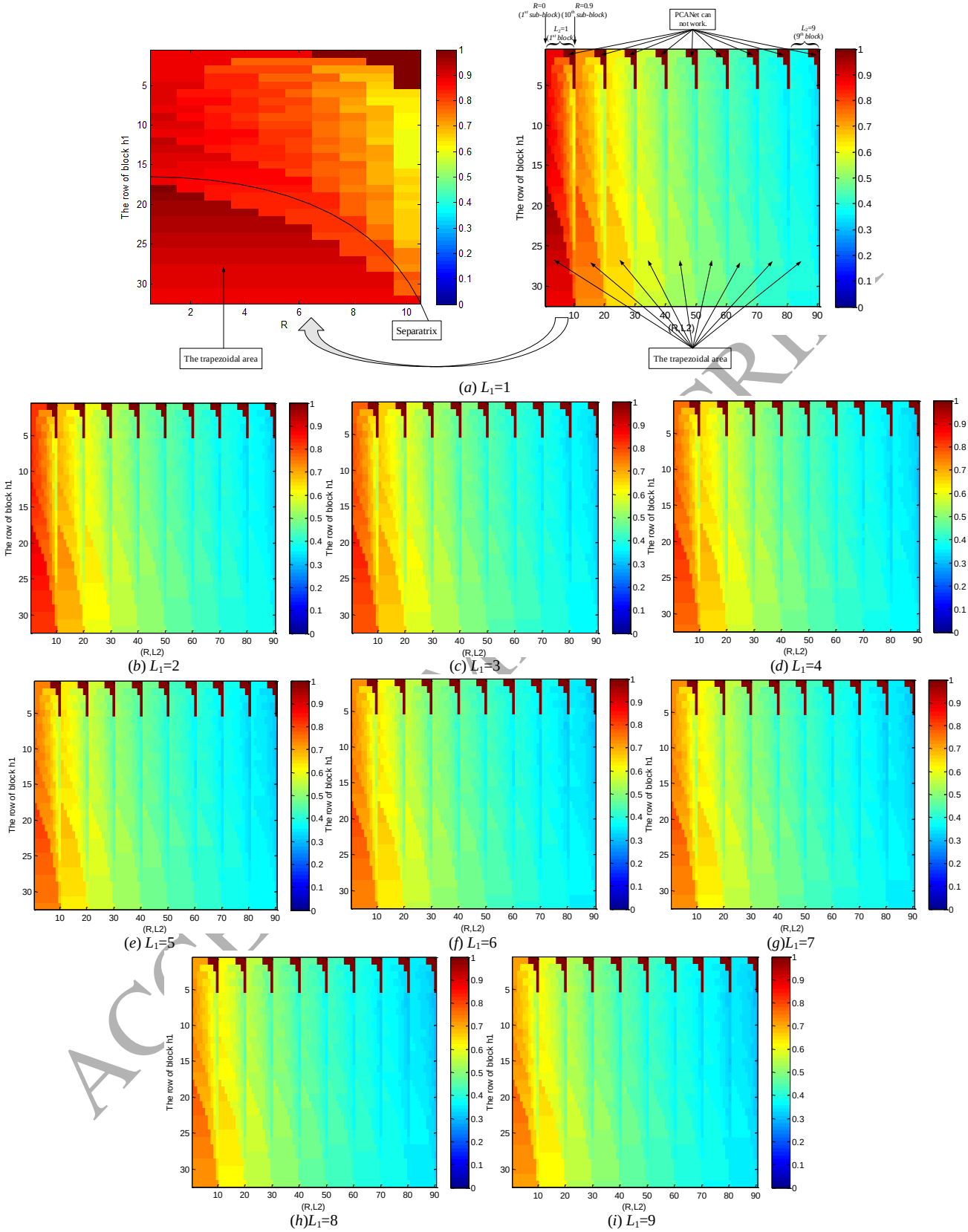

(*a*) L_1=1

(*b*) L_1=2 (*c*) L_1=3 (*d*) L_1=4

(*e*) L_1=5 (*f*) L_1=6 (*g*)L_1=7

(*h*)L_1=8 (*i*) L_1=9

Fig. 2. The inverse of logarithm of BlockEnergy of Yale dataset in relation with h_1, R, L_1, L_2, where $h_1 \in \{1{:}1{:}32\}$, $R \in \{0{:}0.1{:}0.9\}$, $L_1 \in \{1{:}1{:}9\}$, $L_2 \in \{1{:}1{:}9\}$.

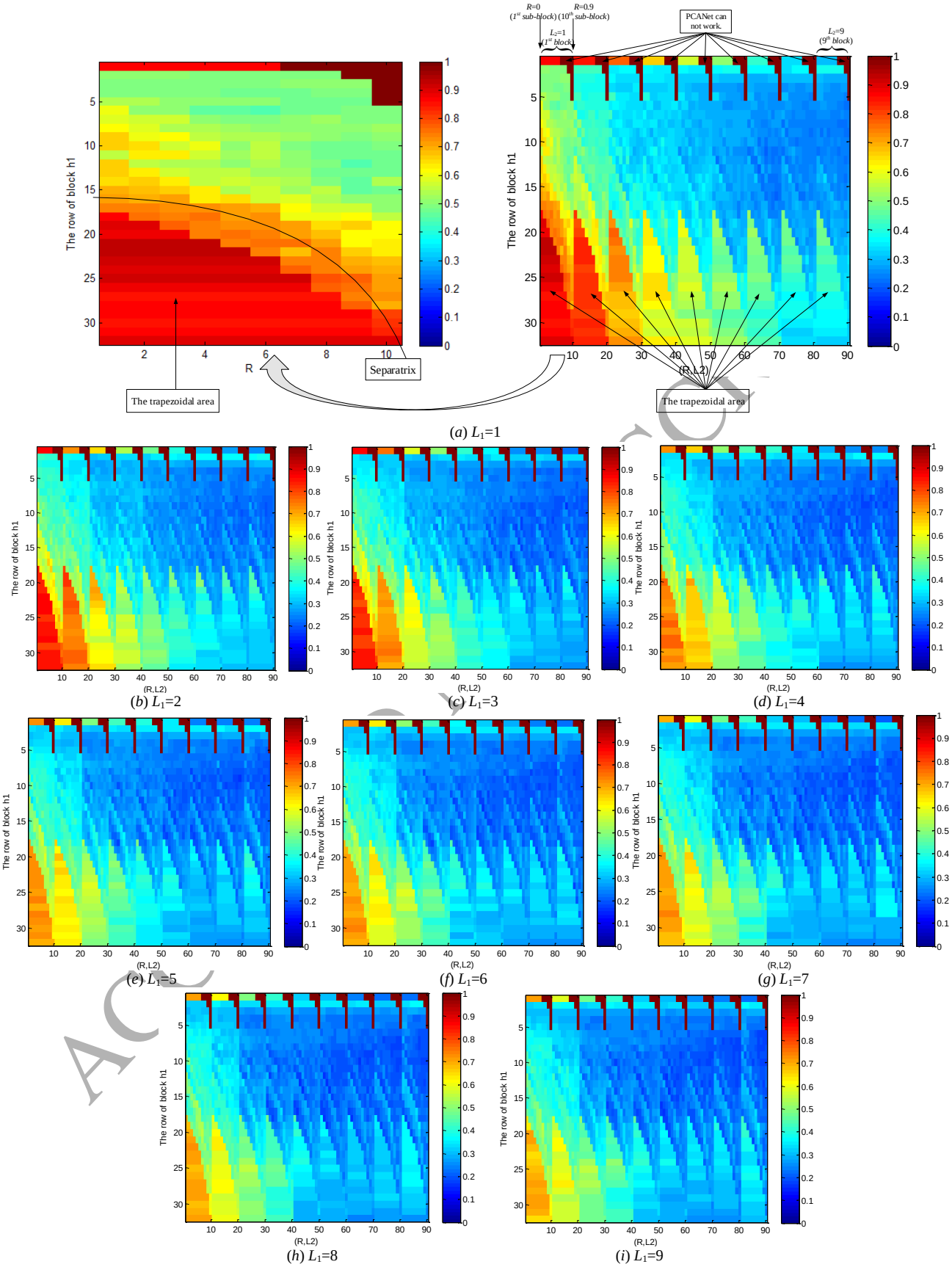

(*a*) L_1=1

(*b*) L_1=2 (*c*) L_1=3 (*d*) L_1=4

(*e*) L_1=5 (*f*) L_1=6 (*g*) L_1=7

(*h*) L_1=8 (*i*) L_1=9

Fig. 3. The error rate *e* of Yale dataset in relation with h_1, R, L_1, L_2, where $h_1 \in \{1{:}1{:}32\}$, $R \in \{0{:}0.1{:}0.9\}$, $L_1 \in \{1{:}1{:}9\}$, $L_2 \in \{1{:}1{:}9\}$.

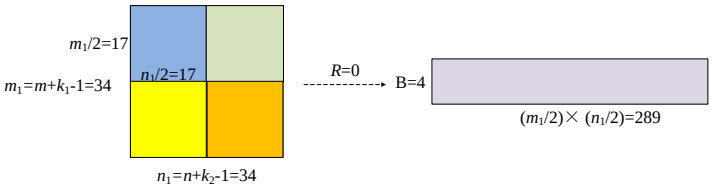

(*a*)

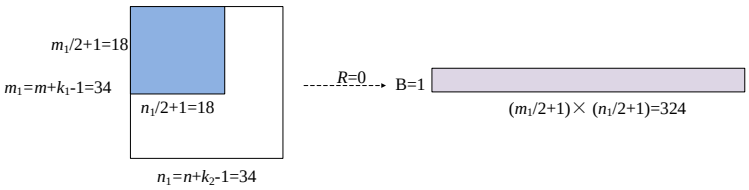

(*b*)

Fig. 4. The illustration of trapezoidal area. (*a*) $h_1=(m+k_1-1)/2$; (*b*) $h_1=(m+k_1-1)/2+1$.

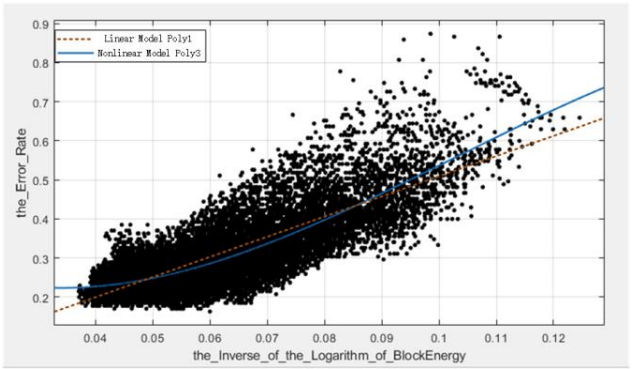

(*a*)

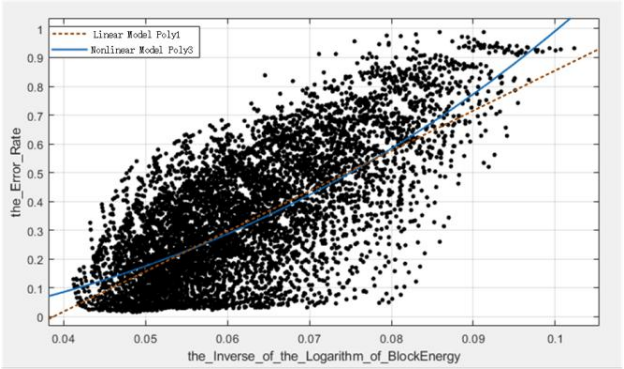

(*b*)

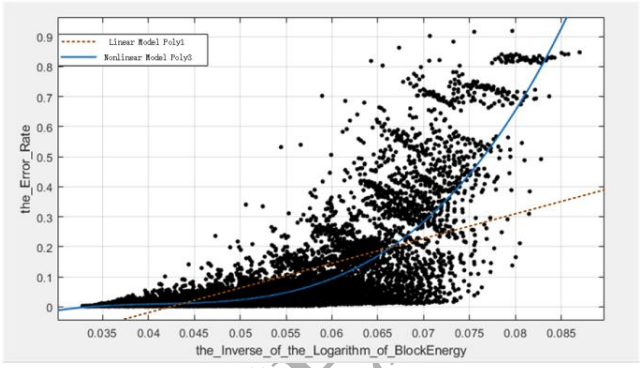

(*c*)

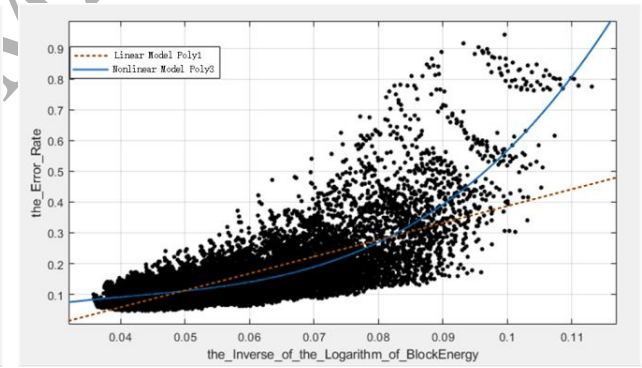

(*d*)

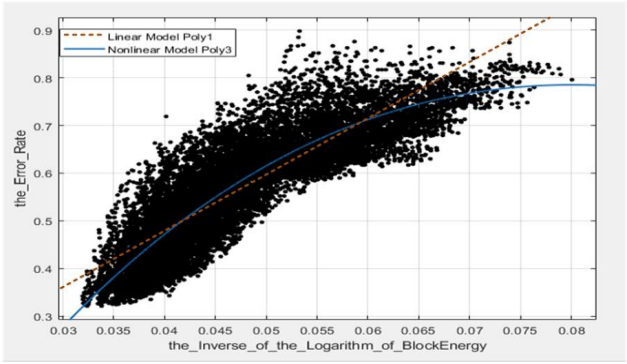

(*e*)

Fig. 5. The curve fitting results for five datasets. (*a*) Yale database; (*b*) AR database; (*c*) CMU PIE database; (*d*) ORL database; (*e*) CIFAR-10 database.

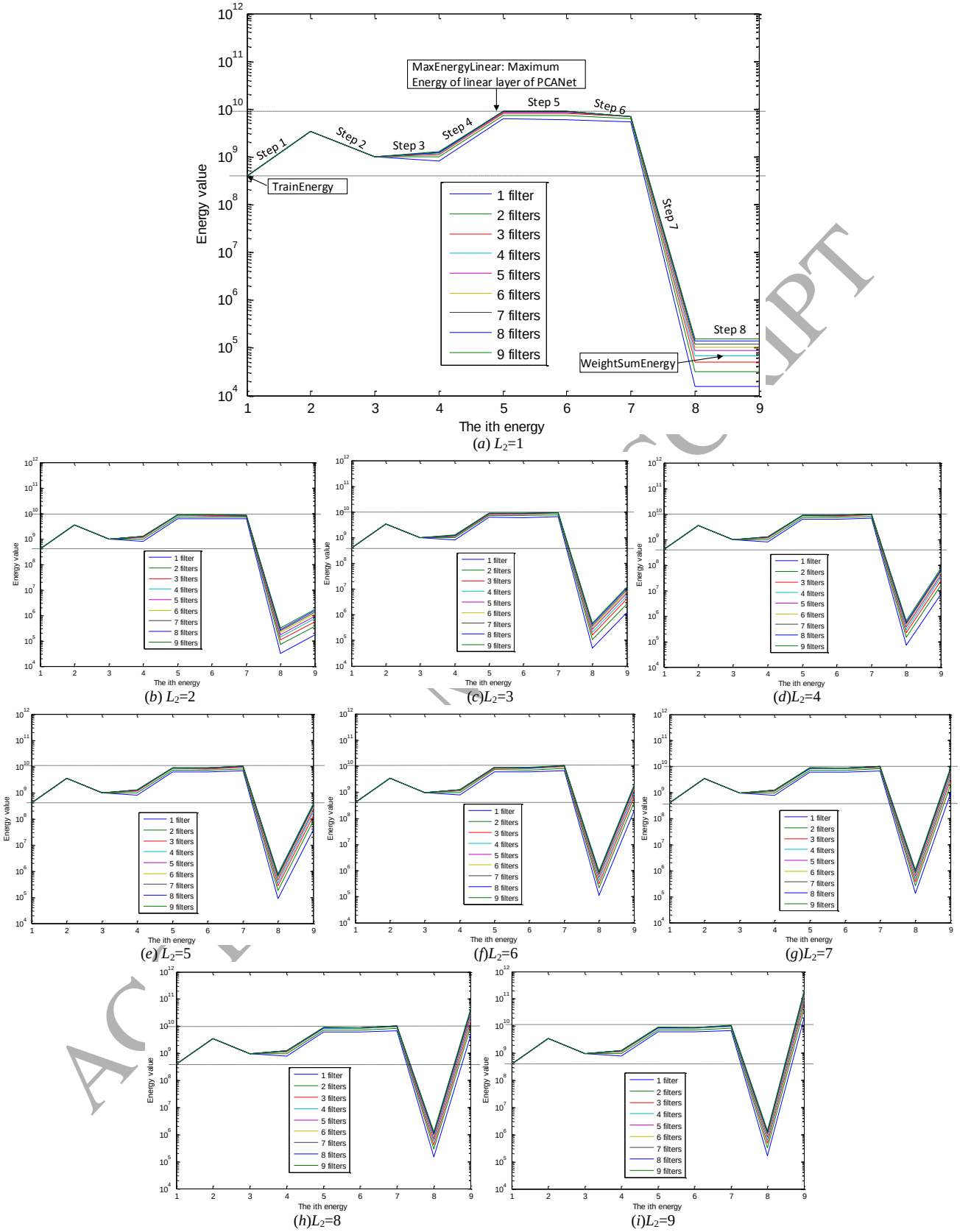

(*a*) L_2=1

(*b*) L_2=2 (*c*)L_2=3 (*d*)L_2=4

(*e*) L_2=5 (*f*)L_2=6 (*g*)L_2=7

(*h*)L_2=8 (*i*)L_2=9

Fig. 6. The energy values of all stages of the first part of PCANet versus the *n*th energy (Yale dataset). The parameters are L_1, $L_2 \in \{1{:}1{:}9\}$.

Table 1. The core parameters of PCANet.

Parameters	Descriptions
$m\times n$	*The size of input image*
$k_1 \times k_2$	*The patch size.* k_1 and k_2 are odd integers and satisfy $1\le k_1\le m$, $1\le k_2\le n$. In this paper, we always set $k_1=k_2=3$.
L_1, L_2	*The number of filters of two stages.* $1\le L_1\le k_1k_2$, $1\le L_2\le k_1k_2$
$h_1 \times h_2$	*The block size.* $1\le h_1\le m$, $1\le h_2\le n$. *Constraint:* $h_2=\lfloor nh_1/m \rfloor$
R	*The overlap ratio of block.* $R\in\{0{:}0.1{:}0.9\}$ *which means R varies from 0 to 0.9 with the interval 0.1.*

Table 2
The energy and error rate of PCANet we recorded and their descriptions.

Two parts	Energy or Error rate	Descriptions
The first part	**TrainEnergy**	The total energy of N input training images. $E(\mathbf{I})=\sum_{j=1}^{m}\sum_{k=1}^{Nn}\mathbf{I}^2(j,k)$, $\mathbf{I}$ is defined in Eq. (1).
	PatchEnergy1	The total energy of N images after the first patch sliding process (Step 1). $E(\mathbf{X})=\sum_{j=1}^{k_1k_2}\sum_{k=1}^{Nmn}\mathbf{X}^2(j,k)$, $\mathbf{X}$ is defined in Eq. (3).
	PatchEnergyRed1	The total energy of N images after the first mean remove process (Step 2). $E(\bar{\mathbf{X}})=\sum_{j=1}^{k_1k_2}\sum_{k=1}^{Nmn}\bar{\mathbf{X}}^2(j,k)$, $\bar{\mathbf{X}}$ is defined in Eq. (5).
	PCAEnergy1	The total energy of NL_1 images after the first PCA process (Step 3) $E(\mathbf{I}^I)=\sum_{j=1}^{m}\sum_{k=1}^{L_1Nn}(\mathbf{I}^I(j,k))^2$, $\mathbf{I}^I$ is defined in Eq. (13).
	PatchEnergy2	The total energy of NL_1 images after the second patch sliding process (Step 4). $E(\mathbf{Y})=\sum_{j=1}^{k_1k_2}\sum_{k=1}^{L_1Nmn}(\mathbf{Y}(j,k))^2$, $\mathbf{Y}$ is defined in Eq. (16).
	PatchEnergyRed2	The total energy of NL_1 images after the second mean remove process (Step 5). $E(\bar{\mathbf{Y}})=\sum_{j=1}^{k_1k_2}\sum_{k=1}^{L_1Nmn}(\bar{\mathbf{Y}}(j,k))^2$, $\bar{\mathbf{Y}}$ is defined in Eq. (17).
	PCAEnergy2	The total energy of NL_1L_2 images after the second PCA process (Step 6) $E(\mathbf{I}^{II})=\sum_{j=1}^{m}\sum_{k=1}^{L_1L_2Nn}(\mathbf{I}^{II}(j,k))^2$, $\mathbf{I}^{II}$ is defined in Eq. (28).
	BinaryEnergy	The total energy of NL_1L_2 images after the binary process (Step 7) $E(\mathbf{P})=\sum_{j=1}^{m}\sum_{k=1}^{L_1L_2Nn}(\mathbf{P}(j,k))^2$, $\mathbf{P}$ is defined in Eq. (30).
	WeightSumEnergy	The total energy of NL_1 images after the weight and sum process (Step 8) $E(\mathbf{T})=\sum_{j=1}^{m}\sum_{k=1}^{L_1L_2Nn}(\mathbf{T}(j,k))^2$, $\mathbf{T}$ is defined in Eq. (32).
The second part	**BlockEnerg**	The total energy of NL_1 images after the block sliding process (Step 9). In relation with the parameters h_1, h_2, and R $E(\mathbf{Z})=\sum_{j=1}^{m}\sum_{k=1}^{L_1L_2Nn}(\mathbf{Z}(j,k))^2$, $\mathbf{Z}$ is defined in Eq. (35).
	ErrorRate	The error rate e of PCANet.

Table 3. The accuracy, time consumption, and dimension of features of PCANet when R varies from 0 to 0.9 in the case of $k_1=k_2=3$, $L_1=L_2=8$, $h_1=h_2=8$ (YALE database)

R	0	0.1	0.2	0.3	0.4	0.5	0.6	0.7	0.8	0.9
Accuracy(%)	0.8074	0.7926	0.7926	0.7926	0.8074	0.8074	0.8148	0.8148	0.8148	0.8148
Time consumption(s)	0.8563	0.8426	1.0479	1.1019	1.4804	1.7399	2.7093	5.9280	6.1109	22.2064
Dimension of features	32768	32768	51200	51200	73728	100352	165888	401408	401408	1492992

Table 4. The data fitting result and its criterions for five databases. Note that $e=f(g)$, $g=1/\log_{10}(E(\mathbf{Z}))$.

Databases	Linear model Poly1				Nonlinear model Poly3			
	Model obtained by data fitting	Error sum of squares (SSE)	R-square	Root mean square error (RMSE)	Model obtained by data fitting	Error sum of squares (SSE)	R-square	Root mean square error (RMSE)
Yale database	e=5.117g-0.008589	69.23	0.6104	0.06276	e=-518.1g^3+159.1g^2 -9.032g+0.367	65.95	0.6288	0.06126
AR database	e= 13.78g-0.5269	239.4	0.4302	0.1751	e=355.1g^3+54.51g^2 +1.935g-0.1016	236.9	0.4363	0.1742
CMU PIE database	e=0.08365g+0.06158	188.9	0.3943	0.1037	e=0.01084g^3+0.0298g^2+0.03435g+0.02453	137.6	0.5587	0.0885
ORL database	e= 0.08561g+ 0.06158	183.1	0.413	0.1021	e=0.00658g^3+0.0305g^2+0.04161g+0.02586	137.2	0.56	0.08837
CIFAR-10 database	e= 11.77g+ 0.006023	65.1	0.7456	0.06262	e=728.1g^3-340.7g^2+ 40.56g-0.6522	57.87	0.7739	0.05904

Table 5. The energy and the cumulative percentage of energy of BlockEnergy corresponding to $R\in\{0{:}0.1{:}0.9\}$. The parameters are $L_1 = L_2 = 8$, $h_1=h_2=8$. (YALE database)

Overlap ratio R	0	0.1	0.2	0.3	0.4	0.5	0.6	0.7	0.8	0.9
The ith filter	1st	2nd	3rd	4th	5th	6th	7th	8th	9th	10th
The energy of corresponding output image ($\times10^{11}$)	2.4398	0.6564	0.6564	0.2725	0.1653	0.1215	0.0844	0.0844	0.0544	0.0542
Energy sum($\times10^{11}$)	2.4398	3.0962	3.7527	4.0252	4.1905	4.3120	4.3964	4.4808	4.5352	4.5893
The cumulative percentage of energy	0.5316	0.6747	0.8177	0.8771	0.9131	0.9396	0.9580	0.9764	0.9882	1.0000

Table 6. The cumulative percentage of energy and the cumulative percentage of eigenvalue of 9 filters (the 1st and the 2nd PCAs). (YALE database)

Parameters	The ith filter	Energy sum($\times10^{10}$)	Cumulative percentage of energy	Eigenvalue ($\times10^4$)	Eigenvalue sum ($\times10^4$)	Cumulative percentage of eigenvalue	Error Rate
$h_1=h_2=8$ R=0.5 L_2=1 $L_1\in\{1{:}1{:}9\}$	1	0.07984	0.6386	2.1544	2.1544	0.6820	0.5037
	2	0.09794	0.7834	0.3884	2.5428	0.8049	0.4519
	3	0.11223	0.8977	0.3330	2.8757	0.9103	0.4370
	4	0.11785	0.9427	0.1151	2.9908	0.9468	0.4370
	5	0.12160	0.9727	0.0789	3.0697	0.9717	0.4148
	6	0.12339	0.9870	0.0466	3.1163	0.9865	0.4000
	7	0.12410	0.9927	0.0189	3.1352	0.9925	0.4000
	8	0.12470	0.9975	0.0152	3.1504	0.9973	**0.3926**
	9	0.12502	1.0000	0.0086	3.1590	1.000	0.4074
$h_1=h_2=8$ R=0.5 L_1=8 $L_2\in\{1{:}1{:}9\}$	1	0.6907	0.6632	2.4729	2.4729	0.6912	0.3926
	2	0.8211	0.7883	0.4369	2.9098	0.8134	0.3185
	3	0.9271	0.8902	0.3658	3.2755	0.9156	0.2593
	4	0.9772	0.9383	0.1232	3.3987	0.9500	0.2519
	5	1.0129	0.9726	0.0871	3.4858	0.9744	0.2370
	6	1.0279	0.9869	0.0514	3.5372	0.9887	0.2074
	7	1.0339	0.9927	0.0188	3.5560	0.9940	0.2000
	8	1.0388	0.9974	0.0155	3.5715	0.9983	**0.1926**
	9	1.0415	1.0000	0.0060	3.5775	1.0000	0.2000

Table 7. The error rate corresponds to L_1, $L_2\in\{1{:}1{:}9\}$ when $h_1=h_2=8$, R=0.5. (YALE database)

L_1/Error rate/ L_2	1	2	3	4	5	6	7	8	9
1	0.5037	0.4370	0.3259	0.3185	0.2963	0.2667	0.2444	0.2444	0.2444
2	0.4519	0.3926	0.2963	0.3111	0.2741	0.2370	0.2370	0.2000	0.2074
3	0.4370	0.3630	0.2963	0.2889	0.2593	0.2519	0.2222	0.2148	0.2000
4	0.4370	0.3481	0.2741	0.2741	0.2593	0.2444	0.2000	0.2074	0.2000
5	0.4148	0.3259	0.2741	0.2815	0.2667	0.2148	0.2222	0.2148	0.2000
6	0.4000	0.3333	0.2815	0.2593	0.2593	0.2222	0.2296	0.2000	0.2074
7	0.4000	0.3259	0.2741	0.2370	0.2519	0.2148	0.2222	**0.1852**	0.1926
8	0.3926	0.3185	0.2593	0.2519	0.2370	0.2074	0.2000	0.1926	0.2000
9	0.4074	0.3259	0.2741	0.2444	0.2370	0.2148	0.2074	0.2000	0.2000

Jiasong Wu received the joint Ph.D. degree with the Laboratory of Image Science and Technology (LIST), Southeast University, Nanjing, China, and Laboratoire Traitement du signal et de l'Image (LTSI), University of Rennes 1, Rennes, France in 2012. He is now working in the LIST as a lecturer. His research interest mainly includes deep learning, fast algorithms of digital signal processing and its applications.

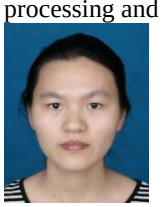

Shijie Qiu received the B.S. degree in Mathematical Science from Soochow University in 2015. Now she is currently pursuing the M.S. degree in Computer Science, Southeast University. Her research interests lie in deep learning and pattern recognition.

Youyong Kong received the B.S. and M.S. degrees in computer science and engineering from Southeast University, Nanjing, China, in 2008 and 2011, respectively, and the Ph.D. degree in imaging and diagnostic radiology from the Chinese University of Hong Kong, Hong Kong, in 2014.He is currently an Assistant Professor with the College of Computer Science and Engineering, Southeast University. His current research interests include machine learning, and medical image processing and brain network analysis.

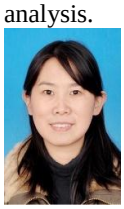

Longyu Jiang received Ph.D. degrees in signal processing from Grenoble University, Grenoble, France, in 2013. Since 2013, she has been a Faculty Member with the Department of Computer Science and Engineering, Southeast University, Nanjing, China. Her major research interest includes MRI image reconstruction, array processing.

Yang Chen received the B.S. degree and Ph.D. degree in Biomedical Engineering from the First Military Medicine University (China) in 2001 and 2007. He is currently an associate professor of the LIST Laboratory in Southeast University, China. His rece nt work concentrates on medical image reconstruction and analysis.

Wankou Yang received his B.S., M.S. and Ph.D. degrees at the School of Computer Science and Technology, Nanjing University of Science and Technology (NUST), PR.China, 2002, 2004 and 2009 respectively. From July 2009 to Sep. 2011, he worked as a postdoctoral fellow at the School of Automation, Southeast University. From Sep. 2011 to March 2016, he worked as an assistant professor at the School of Automation, Southeast University. Now he is an associate professor in the School of Automation, Southeast University, P.R. China. His research interests include pattern recognition, computer vision.

Lotfi Senhadji received the Ph.D. degree from the University of Rennes 1, Rennes, France, in signal processing and telecommunications in 1993. He is a Professor and the Head of the INSERM Research Laboratory LTSI. His is also Co-Director of the French-Chinese Laboratory CRIBs "Centre de Recherche en Information Biomédicale Sino-Français". His main research efforts are focused on nonstationary signal processing with particular emphasis on wavelet transforms and time-frequency representations for detection, classification, and interpretation of biosignals.

Huazhong Shu received the B.S. degree in Applied Mathematics from Wuhan University, China, in 1987, and a Ph.D. degree in Numerical Analysis from the University of Rennes 1, Rennes, France in 1992. He is a professor of the LIST Laboratory and the Codirector of the CRIBs. His recent work concentrates on the image analysis, pattern recognition and fast algorithms of digital signal processing. Dr. Shu is a senior member of IEEE Society.